

# The Microphysical Roles of Lower-Tropospheric versus Midtropospheric Aerosol Particles in Mature-Stage MCS Precipitation

PETER J. MARINESCU, SUSAN C. VAN DEN HEEVER, STEPHEN M. SALEEBY,  
SONIA M. KREIDENWEIS, AND PAUL J. DEMOTT

*Department of Atmospheric Science, Colorado State University, Fort Collins, Colorado*

(Manuscript received 14 December 2016, in final form 17 August 2017)

## ABSTRACT

Simulations of two leading-line, trailing-stratiform mesoscale convective system (MCS) events that occurred during the Midlatitude Continental Convective Clouds Experiment (MC3E) have been used to understand the relative microphysical impacts of lower- versus midtropospheric aerosol particles (APs) on MCS precipitation. For each MCS event, four simulations were conducted in which the initial vertical location and concentrations of cloud droplet nucleating APs were varied. These simulations were used to determine the precipitation response to AP vertical location. Importantly, the total integrated number and mass of the initial aerosol profiles used in the sensitivity simulations remained constant, such that differences in the simulations could be directly attributable to changes in the vertical location of cloud droplet nucleating APs. These simulations demonstrate that lower-tropospheric APs largely influenced the precipitation response directly rearward of the leading cold pool boundary. However, farther rearward in the MCS, the relative impact of lower- versus midtropospheric APs largely depended on the MCS structure, which varied between the two events because of differences in line-normal wind shear. Midtropospheric APs were able to activate new cloud droplets in the midtropospheric levels of convective updrafts and to enhance mixed-phase precipitation through increased cloud riming, and this microphysical pathway had a more significant impact on mixed-phase precipitation in weaker line-normal wind shear conditions. This result exposes the importance of properly representing midtropospheric APs when assessing aerosol effects on clouds. This study also demonstrates the utility of assessing aerosol effects within the different regions of MCSs.

## 1. Introduction

During the warm season in the central United States, mesoscale convective systems (MCSs) are the highest contributors to surface accumulated precipitation (Fritsch et al. 1986). Under certain atmospheric conditions, individual MCS events can also produce widespread and intense precipitation that leads to flooding (e.g., Doswell et al. 1996; Schumacher and Johnson 2005; Stevenson and Schumacher 2014), such as the extreme 1993 floods in the Mississippi valley (Kunkel et al. 1994). As such, understanding changes to MCS precipitation due to perturbations in the environment is important.

Each year, expansive biomass-burning events occur in Mexico and Central America. The wind patterns that are responsible for providing favorable MCS conditions in the central United States during the spring and summer months (i.e., warm and moist air, wind shear) are

also frequently responsible for transporting high aerosol particle (AP) concentrations from these large biomass-burning events in Central America and Mexico into the central United States (Rogers and Bowman 2001; Gebhart et al. 2001; Duncan et al. 2003; Wang et al. 2006). Observations from the Department of Energy's Atmospheric Radiation Measurement Program's Southern Great Plains (ARM-SGP) site (36.6°N, 97.5°W) have shown that biomass-burning APs are frequent in the spring and summer months (Peppler et al. 2000; Sheridan et al. 2001; Andrews et al. 2004). Peppler et al. (2000) further reported that while biomass-burning APs were confined to the boundary layer in the first few weeks of May 1998, later in the month, the biomass-burning APs were observed in a layer between 3 and 6 km, thus demonstrating the variability in the altitude of primary transport pathways. Figure 1 demonstrates an example of the transport of biomass-burning APs into the southern United States both within the lower troposphere and the middle troposphere, as predicted by the Navy Aerosol Analysis and Prediction System

---

*Corresponding author:* Peter J. Marinescu, peter.marinescu@colostate.edu

DOI: 10.1175/JAS-D-16-0361.1

© 2017 American Meteorological Society. For information regarding reuse of this content and general copyright information, consult the [AMS Copyright Policy](http://www.ametsoc.org/PUBSReuseLicenses) ([www.ametsoc.org/PUBSReuseLicenses](http://www.ametsoc.org/PUBSReuseLicenses)).

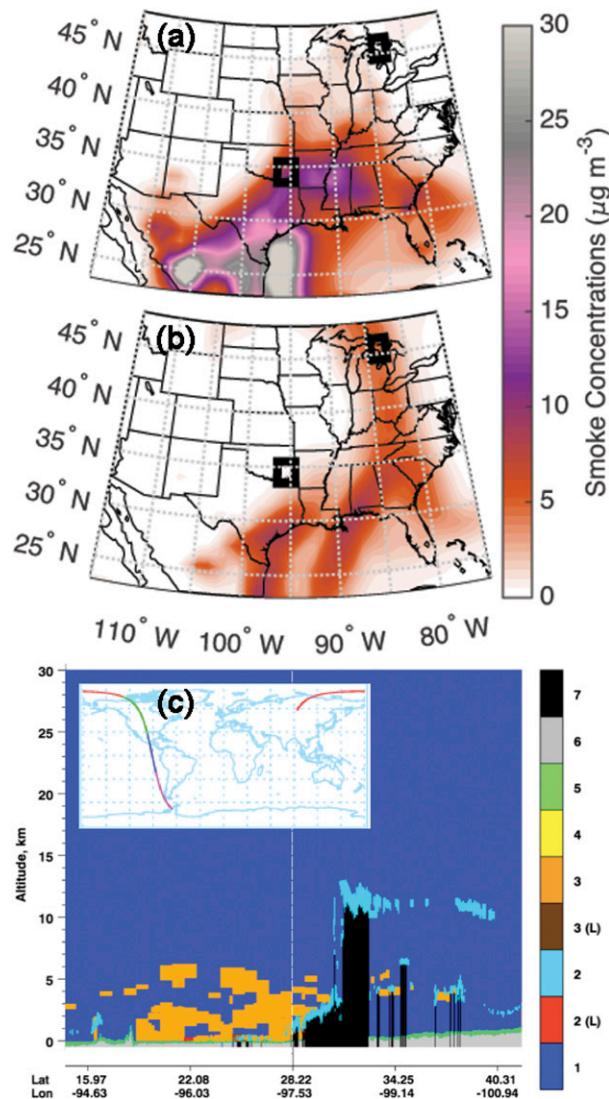


FIG. 1. (a),(b) NAAPS model smoke mass concentrations from 0000 UTC 22 May 2011 at (a)  $\sim 1$  and (b)  $\sim 5$  km AGL. The black boxes represent the areas used to create sensitivity aerosol profiles for the model initialization, as described in section 2b. (c) CALIPSO lidar vertical feature mask, version 3.01, at  $\sim 2000$  UTC 20 May 2011. The shaded regions in (c) represent clean air (1); cloud (2); cloud, low confidence (2L); aerosol (3); aerosol, low confidence (3L); stratospheric layer (4); surface (5); subsurface (6); and totally attenuated regions (7). The global map inset shows the satellite track, with the image here falling between the blue and green tracks. [This image in (c) is from <http://www-calipso.larc.nasa.gov/>.]

(NAAPS; Figs. 1a,b) and as observed in satellite measurements from CALIPSO (Fig. 1c). Furthermore, there can be regions with higher concentrations of transported aerosol particles in the middle troposphere as compared to the lower troposphere (such as over the Great Lakes region in Figs. 1a and 1b). This influx of biomass-burning APs into the central United States has also been

suggested by numerous studies to be linked to an increased frequency and intensity of severe weather in the region, although these studies have focused more on lightning, hail, and tornadoes and less on the impacts of APs on MCS precipitation (Lyons et al. 1998; Murray et al. 2000; Wang et al. 2009; Saide et al. 2015, 2016).

Most modeling studies that have focused on the impact of AP concentration perturbations on MCS precipitation have been conducted by running a suite of simulations, in which the number concentrations of aerosol particles near the surface or throughout the total atmospheric column were altered by some factor (Tao et al. 2007; Li et al. 2009; Lebo and Morrison 2014). These studies have shown that under increased aerosol concentrations, MCS total surface accumulated precipitation can increase, decrease, or remain relatively unchanged. The differences in precipitation response to aerosol particles may be due to many factors, including differences in the model configurations used in the respective studies (e.g., grid spacing, physical parameterizations) and differences in the environmental factors of the MCS events simulated (Tao et al. 2012), such as tropospheric relative humidity (Tao et al. 2007) or wind shear (Lebo and Morrison 2014).

On the other hand, only a couple of studies (Fridlind et al. 2004, hereinafter F04; Lebo 2014, hereinafter L14) have assessed how the vertical variation of aerosol particle number concentrations impacts deep convection, which is especially relevant in regions where mid- and upper-tropospheric concentrations of aerosol particles can vary significantly (e.g., regions impacted by the long-range transport of aerosol particles). Furthermore, aerosol particles in the middle or upper troposphere may be particularly important for aerosol–cloud interactions within MCSs (Fan et al. 2016). Using both simulations and measurements from the Cirrus Regional Study of Tropical Anvils and Cirrus Layers–Florida–Area Cirrus Experiment (CRYSTAL-FACE), F04 demonstrated that midtropospheric aerosol particles can become entrained into strong, convective updrafts and impact the cloud droplet spectrum and anvil properties in tropical convection. L14 used idealized numerical simulations of a squall line to assess the impact of the vertical location of aerosol particles on many aspects of a squall line, including precipitation. In L14, the simulation that was initialized with high concentrations of aerosol particles in the middle and upper troposphere was most similar to the simulation with high aerosol particle concentrations throughout the entire atmospheric column in terms of precipitation and MCS structure (e.g., convective updraft mass flux, hydrometeor amounts), thus suggesting that perturbations to the midtropospheric aerosol concentrations may have a

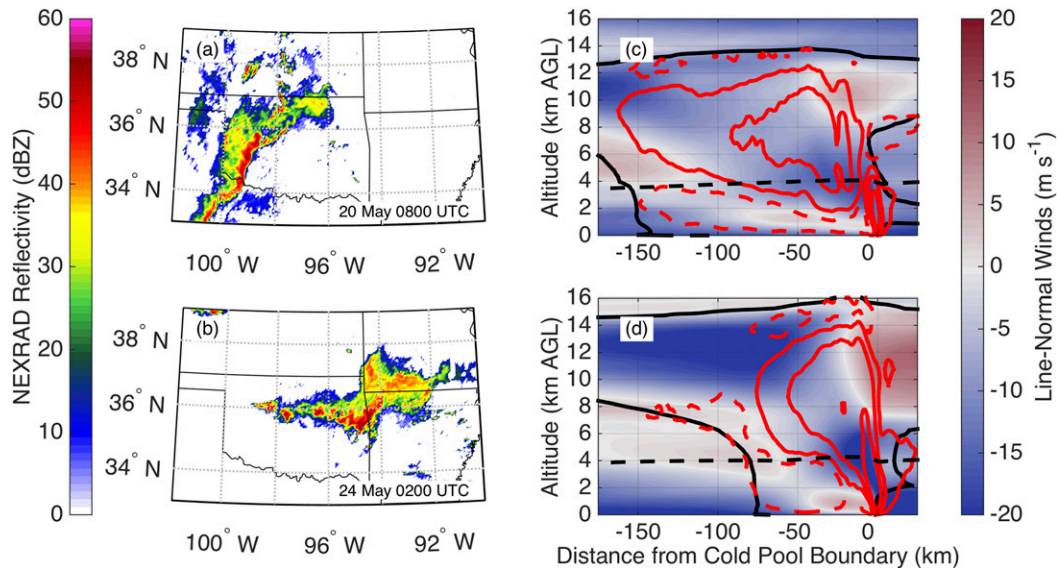


FIG. 2. (left) NEXRAD reflectivity at 2.5 km AGL at (a) 0800 UTC 20 May and (b) 0200 UTC 24 May 2011. (right) As described in section 2c, composite cross sections during the mature stage of the simulated MCSs for the (c) 20 and (d) 24 May events are also shown. In these cross sections, storm-relative, convective-line-normal horizontal winds ( $\text{m s}^{-1}$ ) are shaded; updrafts (0.25, 1, and  $3 \text{ m s}^{-1}$ ) have red solid contours; downdrafts ( $0.1 \text{ m s}^{-1}$ ) have red dashed contours; and total condensate ( $0.1 \text{ g kg}^{-1}$ ) has a black solid contour. The  $0^\circ\text{C}$  temperature level is shown with a dashed, black line. It is assumed that the MCSs are moving at  $14$  and  $18 \text{ m s}^{-1}$  for the 20 and 24 May events, respectively, which are based on the leading cold pool boundary detection described in section 2c.

more significant impact on MCS intensity than perturbations to the lower-tropospheric aerosol concentrations. However, one limitation of L14 is that the vertically integrated aerosol mass was not constant between the sensitivity aerosol profiles, such that the initial aerosol profile with greater particle concentrations in the middle and upper troposphere had  $\sim 1.8$  times more vertically integrated aerosol mass than the profile with peak aerosol concentrations in the lower troposphere. As such, the differences between the L14 simulations could be partly attributed to the differences in aerosol mass and number present in the middle and upper troposphere rather than solely to the vertical location of aerosol particles.

In this study, we compare the results of simulations in which the vertical location of the aerosol used to initialize the simulation was varied. These sensitivity simulations were used to assess the relative roles of midtropospheric and lower-tropospheric cloud droplet nucleating aerosol particles in MCS precipitation during the mature stage. It should be noted that the initial vertically integrated aerosol total mass and number were constant among the sensitivity simulations. Therefore, differences between the simulations are more directly attributable to the changes in the vertical locations of the peak aerosol concentrations rather than to the differences in the total aerosol number

concentrations. Furthermore, simulations conducted in this study represent two MCS events that occurred during the Midlatitude Continental Convective Clouds Experiment (MC3E; Jensen et al. 2016) and within a period of expansive biomass burning in Mexico and Central America (Fig. 1). Therefore, both the simulations and sensitivity aerosol profiles used in this study were constrained by observations obtained during MC3E, as described in sections 2a and 2b.

The focus of this study is on the mature stage of two MCS events that occurred on 20 and 24 May 2011 (Figs. 2a,b). The 20 May MCS approximately propagated eastward across Oklahoma, while the 24 May MCS event approximately propagated to the southeast into Arkansas. The mature stage was chosen for two primary reasons. First, the majority of MCS precipitation falls during this stage with significant contributions from both the convective and stratiform regions (e.g., Houze 1977; Watson et al. 1988). Second, both MCS events displayed leading-line, trailing-stratiform (LLTS) MCS characteristics during the mature stage (Fig. 2), which allowed for better comparisons between the two events. This study builds on simulations presented in Marinescu et al. (2016), which compared the simulations of the two MCS events to a suite of observations and determined the latent heating rates and latent heating evolution within the different MCS regions,

and in Saleeby et al. (2016), which focused on the impacts of lower-tropospheric aerosol loading on MCS anvil characteristics.

## 2. Experimental design

### a. Model description

Simulations of the two MCS events were conducted with the Regional Atmospheric Modeling System (RAMS). RAMS is a 3D, nonhydrostatic model that utilizes a two-moment, bin-emulating bulk microphysical parameterization that prognoses eight hydrometeor species (Walko et al. 1995; Meyers et al. 1997; Cotton et al. 2003; Saleeby and Cotton 2004; Saleeby and van den Heever 2013). This bin-emulating scheme segments the assumed hydrometeor distributions into bins before calculating several microphysical process rates (e.g., hydrometeor collision–collection and sedimentation) through the use of lookup tables. The use of such a bin-emulating parameterization scheme thus represents some of the sophistication of bin techniques while still applying the computational efficiency of a bulk scheme, although for some conditions, the hybrid approach may not improve hydrometeor sedimentation compared to standard bulk approaches (Morrison 2012). The model is initialized with AP number concentrations at each model grid point, with the same underlying AP size distribution throughout the domain. APs are advected by the model-predicted winds and are available to act as cloud condensation nuclei (CCN), which can be activated to form cloud droplets based on the specified particle sizes and hygroscopicity, as well as the model-predicted environmental conditions, including vertical velocity, temperature, and AP number concentrations (Saleeby and van den Heever 2013). APs can be removed via cloud droplet nucleation, wet scavenging, and dry deposition and can be returned to the atmosphere via the evaporation and sublimation of hydrometeors (Saleeby and van den Heever 2013). RAMS also computes ice nucleation from specified profiles of potential ice nucleating particles (INPs).

In these experiments, vertical profiles of AP concentrations were initialized horizontally homogeneously across the model domain. No additional sources of APs were introduced throughout the simulation time period, although particles were allowed to advect between model grids. The APs used in all of the simulations were specified to have a soluble mass fraction of 0.2 (corresponding to a hygroscopicity parameter  $\kappa$  of 0.15) and to follow a lognormal distribution for the number concentrations with a geometric mean diameter of 120 nm and a standard deviation  $\sigma_g$  of 1.8. These values were

determined in a manner such that the integrated log-normal aerosol distribution matched both CCN number concentration measurements and chemical speciation measurements at the ARM-SGP site during MC3E polluted periods. INP concentrations for all simulations were initialized horizontally homogeneously with the same vertically varying profile of potential INPs. The INP profile was based on vertical profiles of aerosol particle concentrations with diameters larger than 500 nm from airborne observations during MC3E, as well as surface concentrations of aerosol particles with diameters larger than 500 nm at the ARM-SGP site, as described in Saleeby et al. (2016). These INPs were activated in the model simulations based on the ice nucleation scheme developed in DeMott et al. (2010). APs were not allowed to be radiatively active in order to isolate the microphysical impacts of aerosol particles on MCS precipitation.

Simulations were conducted with three nested grids, with the innermost grid (grid 3) spanning from approximately 33° to 40°N and from 102° to 89°W with 1.2-km horizontal grid spacing (Fig. 3). The outermost (grid 1) and middle (grid 2) model grids had 30- and 6-km horizontal grid spacing, respectively. Grids 1–3 had 60 vertical levels with maximum vertical grid spacing of 500 m in the middle and upper troposphere. The Final Global Data Assimilation System (GDAS FNL) reanalysis data from 20 May 2011 were used to initialize and provide lateral boundary conditions for the 20 May event, while the higher-resolution Rapid Update Cycle (RUC) analysis data were used for the 24 May event, since the 24 May event was initially forced by mesoscale features, as described in Marinescu et al. (2016). The simulations were initialized at 0000 and 1600 UTC, respectively, and the results presented in this manuscript represent a 4-h period during the mature stage of both simulated MCSs. These mature-stage periods were 0000–0400 UTC 24 May and 0600–1000 UTC 20 May. Additional details about the simulation dimensions, initialization datasets, and model parameterizations can be found in Table 1 of Marinescu et al. (2016).

Several studies have demonstrated by using idealized simulations of squall lines that the structure of the leading-line convection may be dependent on the model grid spacing (Bryan et al. 2003; Bryan and Morrison 2012; Lebo and Morrison 2015). As such, higher-resolution simulations were completed with 300-m horizontal grid spacing and 85 vertical levels to determine whether the main findings from the original simulations are consistent with simulations with finer model grid spacing. The vertical grid spacing for these higher-resolution simulations ranged from 75 m at the surface to 300 m around 3.5 km AGL, above which it

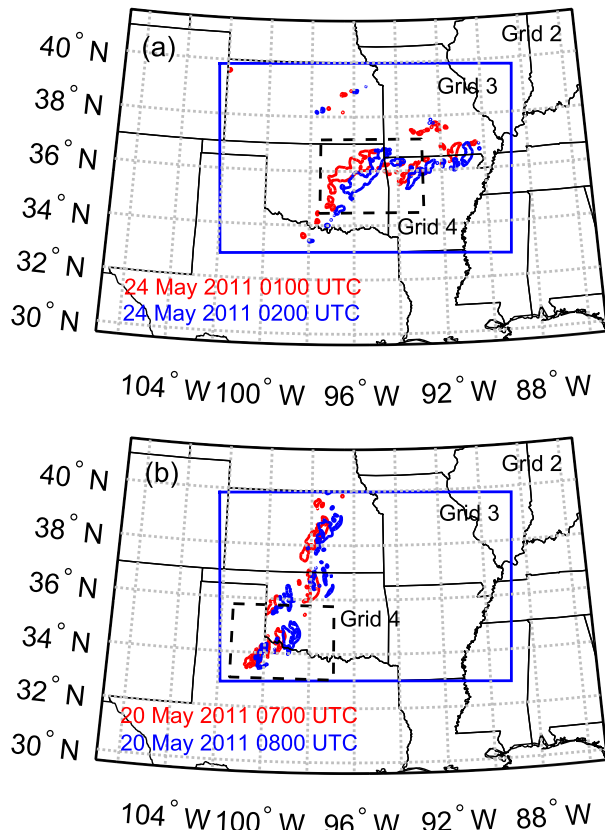


FIG. 3. Simulation domains for the (a) 24 and (b) 20 May events. The entire map represents the domain for grid 2 (6-km horizontal grid spacing), the blue solid box represents the domain for grid 3 (1.2-km horizontal grid spacing), and the black dashed box represent the domain for the additional simulations with 300-m horizontal grid spacing (grid 4). The red and blue contours represent precipitation rates greater than  $15 \text{ mm h}^{-1}$  from the MT simulations (see section 2b) with 1.2-km horizontal grid spacing to demonstrate the location choice of grid 4. Note grid 1 is not shown and covers most of the continental United States and Mexico.

remained constant at 300 m. These simulations were run for 1 h during the mature stage, starting at 0700 and 0100 UTC for the 20 and 24 May events, respectively. The higher-resolution simulations were run over a subset of the original simulations (grids 4 in Fig. 3), and the original simulations were used to initialize and force the lateral boundaries of these additional simulations. The results from the higher-resolution simulations were largely consistent with the original simulations and are further discussed in section 6.

### b. Aerosol sensitivity profiles

For each MCS event, four simulations were conducted that varied the initial, horizontally homogenous, AP concentration vertical profile. These four profiles are displayed in Fig. 4a. The control case (CTL; black line)

utilized a profile that had surface AP number concentrations of  $2000 \text{ cm}^{-3}$  and that decreased the AP number concentration exponentially with a scale height of 7 km. This exponential profile was chosen to represent a typical background profile that may occur in this region during this time period and was approximated based on data from several aircraft research flights during MC3E (Figs. 4b,c). These are the same datasets used by Fridlind et al. (2017), who examined the MC3E aerosol data in a comprehensive manner. Two types of aerosol data are shown from ascent and descent profiles collected by the University of North Dakota Citation aircraft. First, condensation particle counter (CPC; TSI-3771) data (Heymsfield et al. 2014) were examined (Fig. 4b). These data can include particles as small as  $0.01 \mu\text{m}$  (10 nm) that may not readily serve as CCN and occur less homogeneously (Fridlind et al. 2017). Therefore, we also plot ultrahigh sensitivity aerosol spectrometer (UHSAS; Droplet Measurement Technologies) data (Tomlinson et al. 2012) in Fig. 4c, which represent aerosol particles at sizes in the range from  $0.06 \mu\text{m}$  (60 nm) to  $1 \mu\text{m}$ , a typical size range for CCN. Both CPC and UHSAS data were collected at ambient conditions, although the CPC data were sampled via an inlet, while the UHSAS instrument was wing mounted. In both cases, we have applied cloud filtering, similar to Fridlind et al. (2017). Both instruments were not always operating on the same flights. We used a threshold cloud droplet concentrations of  $1 \text{ cm}^{-3}$  from the Droplet Measurement Technologies cloud droplet probe and, in some cases (e.g., for ice clouds), utilized additional threshold conditions on the Particle Measuring Systems two-dimensional cloud (2DC) probe ( $25\text{--}1600 \mu\text{m}$ ) number concentrations ( $>0.01 \text{ cm}^{-3}$ ) and Nevzorov total water content ( $>0.005 \text{ g m}^{-3}$ ) to screen against cloud particle and rain contamination of the CPC and UHSAS data. Nevertheless, there may remain some cloud contamination in the final profiles. The profiles indicate elevated aerosol layers in some cases. The surface aerosol concentrations used for the CTL simulations were based on CCN number concentrations measured at 1% supersaturation from ARM-SGP at the onset of both events (Fig. 5). Note that these values are consistent with the UHSAS data for particles in the  $0.06\text{--}1\text{-}\mu\text{m}$  size range. In the hours leading up to both MCS events, the CCN concentrations measured at ARM-SGP were relatively constant. They subsequently decreased sharply in association with precipitation at the ARM-SGP. To keep the AP initializations consistent among the different events,  $2000 \text{ cm}^{-3}$  was used as a representative surface AP concentration for the CTL simulations for both the 20 and 24 May MCS events. Recall, these profiles (Fig. 4a) represent the initial aerosol conditions within the RAMS model, which subsequently advects, processes, and activates aerosol particles based on prognosed meteorological conditions.

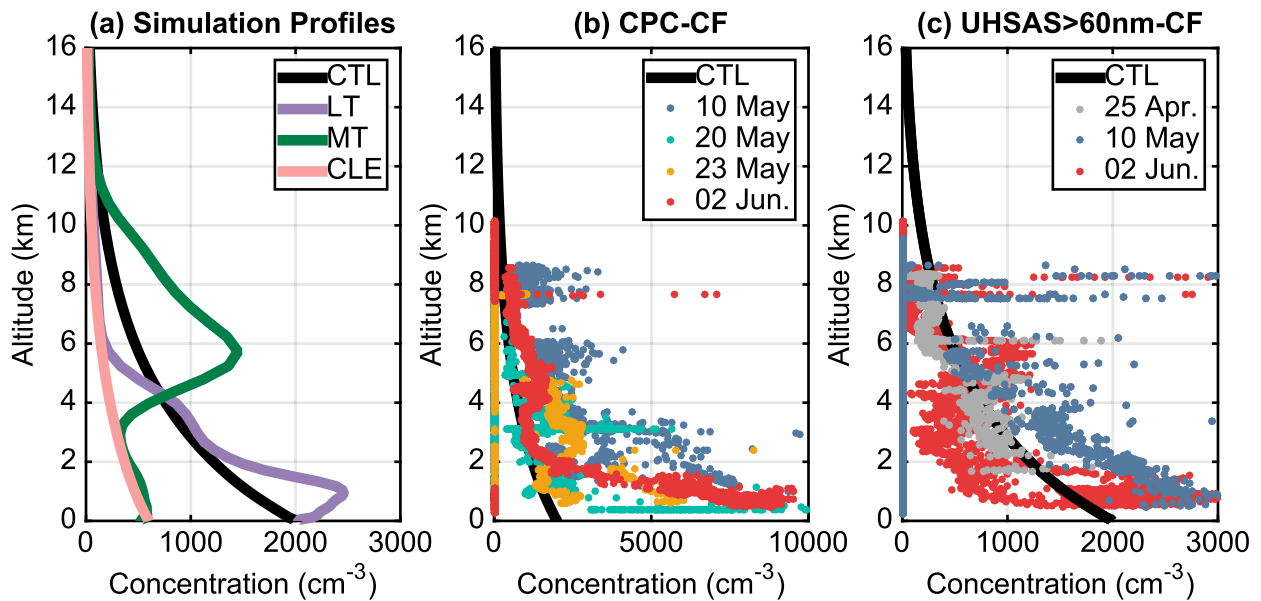


FIG. 4. (a) Vertical profiles of the number concentrations of APs that can serve as cloud condensation nuclei used at model initialization for the sensitivity simulations. CTL represents the AP used for the control simulation, which uses an exponentially decreasing vertical profile with  $2000 \text{ cm}^{-3}$  at the surface. LT and MT represent APs that have peaks in the lower troposphere and middle troposphere, respectively, and have the same total integrated aerosol mass (and number) as the CTL profile. CLE represents a relatively clean, exponentially decreasing AP with similar AP concentrations to the MT profile in the lower troposphere. (b) The CTL profile overlain with 1-Hz cloud-filtered (CF) CPC number concentrations (see main text) and (c) 1-Hz CF UHSAS number concentrations at sizes larger than 60 nm and up to the  $1\text{-}\mu\text{m}$  upper limit of this probe.

Thus, the concentrations of APs are not necessarily equal to the concentrations of activated cloud droplets.

Profiles in which the AP concentrations in the lower-tropospheric (LT) and midtropospheric (MT) levels were enhanced (Fig. 4a) were used to test the impacts of having the majority of the AP number concentrated in the lower troposphere ( $\sim 0\text{--}3$  km AGL) or in the middle troposphere ( $\sim 4\text{--}9$  km AGL). The LT and MT profiles have the same vertically integrated AP mass as the CTL profile, and therefore, changes between the simulations can be directly attributed to changes in the vertical location of AP concentrations as opposed to the changes in the total amount of AP mass (or number). Simulated aerosol fields during MC3E from NAAPS were used to develop the LT and MT profiles, since vertical profiles of aerosol concentrations are difficult to observe. NAAPS is a global aerosol forecast model that predicts the mass concentrations for several different aerosol types, including smoke/soot and sulfate. A detailed description of the NAAPS model and the resulting aerosol dataset is provided in Witek et al. (2007) and Lynch et al. (2016). On 0000 UTC 22 May 2011, NAAPS predicted a smoke plume entering the central United States from Central America and Mexico. Average vertical profiles of smoke/soot and sulfate mass concentrations were calculated over a  $2^\circ \times 2^\circ$  area from the NAAPS output.

These average profiles were determined in two different regions of the central United States in order to better represent the range of the aerosol profiles that an MCS may encounter (see Fig. 1). The average profiles were divided by the total vertically integrated aerosol mass within the profile to create a mass weighting at each level, and these weightings were then applied to the total integrated AP mass from the CTL profile in order to ensure that the total column-integrated AP mass (and number) was constant between the three sensitivity AP profiles (CTL, LT, and MT) at initialization.

A fourth profile was used that had relatively clean AP concentrations throughout the vertical profile (CLE; pink line) with  $\sim 70\%$  less total integrated aerosol mass (and number) than the CTL, LT, and MT profiles. Since this CLE profile had very similar aerosol concentrations to the MT profile from the surface to  $\sim 3$  km AGL, microphysical features that occur in the MT simulations that are significantly different from the CLE simulations can be used to infer the relative impact of midtropospheric APs on the MCS.

### c. Cross-sectional analysis

The mesoscale airflows and structure of mature LLTS MCSs can often be approximated as two-dimensional (e.g., Rutledge and Houze 1987; Fovell and Ogura 1988).

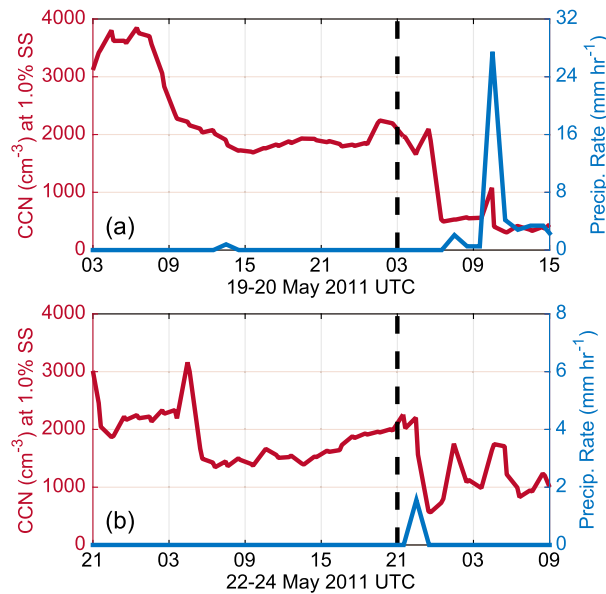


FIG. 5. Time series of CCN number concentrations measured at approximately 1.0% supersaturation (SS) and precipitation rate at the ARM-SGP site for the (a) 20 and (b) 24 May events. The dashed black line represents the approximate time when the initial storms from both MCS events began to form in the region.

Therefore, cross sections through MCSs are frequently used to create a simplified diagnostic to develop an understanding of the kinematic and microphysical processes within the different regions of these systems. In this study, composite cross sections during the mature stage of the simulated MCSs were created relative to the propagating cold pool boundary. The leading cold pool boundary was determined in the model data based on wind shifts and gradients in density potential temperature  $\theta_\rho$ . Density potential temperature is defined as

$$\theta_\rho = \theta \frac{(1 + r_v/\varepsilon)}{(1 + r_T)}, \quad (1)$$

where  $\theta$  is the potential temperature (K),  $r_v$  is the water vapor mixing ratio ( $\text{kg}_{\text{water}} \text{kg}_{\text{air}}^{-1}$ ),  $r_T$  is the total water mixing ratio ( $\text{kg}_{\text{water}} \text{kg}_{\text{air}}^{-1}$ ), and  $\varepsilon$  is 0.622 and represents the ratio of the dry-air gas constant to the water vapor gas constant.

Both wind shifts and temperature gradients are commonly associated with cold pool passages and have been used to identify leading cold pool boundary (gust front) propagations in observations (e.g., Charba 1974; Wakimoto 1982; Engerer et al. 2008). For these simulations, the cold pool boundary was defined at locations that had a surface wind direction shift greater than 45° over a 10-min period and a surface  $\nabla\theta_\rho$  that was greater than a specified threshold that varied depending on the

cold pool lifetime (i.e., the lowest threshold values were associated with the decaying stages of the MCS event). The  $\nabla\theta_\rho$  threshold at each model output time (5-min intervals) was calculated based on the median of the  $\nabla\theta_\rho$  values at the cold pool boundary locations at the prior output time. To prevent localized fluctuations in the intensity of the MCS and cold pool to impact the boundary classification at the next output time, the median  $\nabla\theta_\rho$  value was multiplied by 75%, and the resulting  $\nabla\theta_\rho$  thresholds ranged between 1.5 and 0.1  $\text{K km}^{-1}$ .

Since MCS cold pool boundaries can often extend for several hundred kilometers, an along-boundary cold pool center was determined in order to ensure that the composite cross sections were calculated on similar samples along the detected cold pool boundary in each of the simulations. This cold pool boundary center was based on the centroid of  $\theta_\rho$  behind the cold pool boundary and at 500 m AGL and, therefore, focused the cross-sectional analysis on the most intense region of the cold pool in each simulation at each model output time. This methodology is similar to Trier et al. (2006), who used the approximate centroids of composite radar reflectivity as an estimate of the leading line convection to determine the center location for cross-sectional computations for many MCSs. In this study, this centroid calculation was confined to a 10-km distance perpendicular to the propagation direction from the center point at the prior model output time (5 min). Therefore, it was assumed that the cold pool center point does not move more than 5 km in the along-line direction during the 5-min period between simulated data output. This confinement ensured that a continuous evolution of the same region of the cold pool was assessed. The initial location of the cold pool boundary center point was specified at the same latitude–longitude location at the first analysis time for all of the sensitivity simulations, since the cold pool location is nearly identical among the simulations at these early stages. Once the cold pool boundary was determined, composite cross sections relative to the cold pool boundary were created. These cross sections were generated by first averaging over 100 km in the along-boundary direction and centered at the calculated cold pool boundary center point and then averaging the cross sections temporally over a 4-h time period, during the mature stage of the MCS events, as determined in Marinescu et al. (2016). These time periods were 0600–1000 UTC for the 20 May event and 0000–0400 UTC for the 24 May event. The cross sections extended 250 km behind the cold pool boundary and 100 km ahead of the cold pool boundary, thus creating a 100 km  $\times$  350 km subdomain that traveled with the leading edge of the MCS convective line. Cross sections

created from data within this subdomain were used in the following analysis.

### 3. MCS event on 24 May 2011

#### a. Precipitation cross section

The mean hourly precipitation rates for the suite of 24 May simulations are shown as cross sections in Figs. 6a and 6b. A composite cross section of vertical motions and rain mixing ratios for the CTL simulation is shown in Fig. 6c as a context for the MCS structure, which was largely similar among all the sensitivity simulations. Cross sections were subjectively partitioned into regions (I, II, and III) based on the different dominant microphysical pathways that produced the majority of precipitation within each region, and mean precipitation rates within these regions for the simulations are summarized in Table 1. These pathways are discussed in greater detail in the next section. Within the first  $\sim 15$  km behind the leading cold pool boundary (region I), which accounted for 18%–21% of the total cross-sectional precipitation, the MT and CLE simulations had similar precipitation rates; the mean precipitation rates, averaged across region I in MT and CLE, were  $\sim 15\%$  and  $\sim 25\%$  larger than the LT and CTL simulations, respectively. However, the MT simulation had the highest mean precipitation rate ( $\sim 5\%$ – $10\%$  larger than LT, MT, and CTL) between 15 and 35 km behind the leading cold pool edge (region II), with this region providing 42%–47% of the total precipitation. Last, the region between 35 and 100 km behind the leading cold pool edge (region III) accounted for 33%–37% of the total cross-sectional precipitation. The mean precipitation rate averaged across region III in the CLE and MT simulations were, respectively,  $\sim 9\%$  and  $\sim 5\%$  higher than the mean region III precipitation rate in the CTL simulation. When assessing the total cross-sectional precipitation, the percentage differences from the CTL simulation were  $-1\%$ ,  $+11\%$ , and  $+7\%$  for the LT, MT, and CLE simulations, respectively. Throughout the cross section, the MT precipitation generally differed from the LT and CTL precipitation and compared more closely with the CLE precipitation. This result therefore suggests that the lower-tropospheric aerosol concentrations have a larger impact on MCS precipitation than midtropospheric aerosol concentrations for this suite of sensitivity experiments, since the primary difference between the CLE/MT simulations and the LT/CTL simulations was the concentration of lower-tropospheric aerosol particles (recall Fig. 4a).

#### b. Microphysical processes

To explain these precipitation results, microphysical process rates along the composite cross sections were

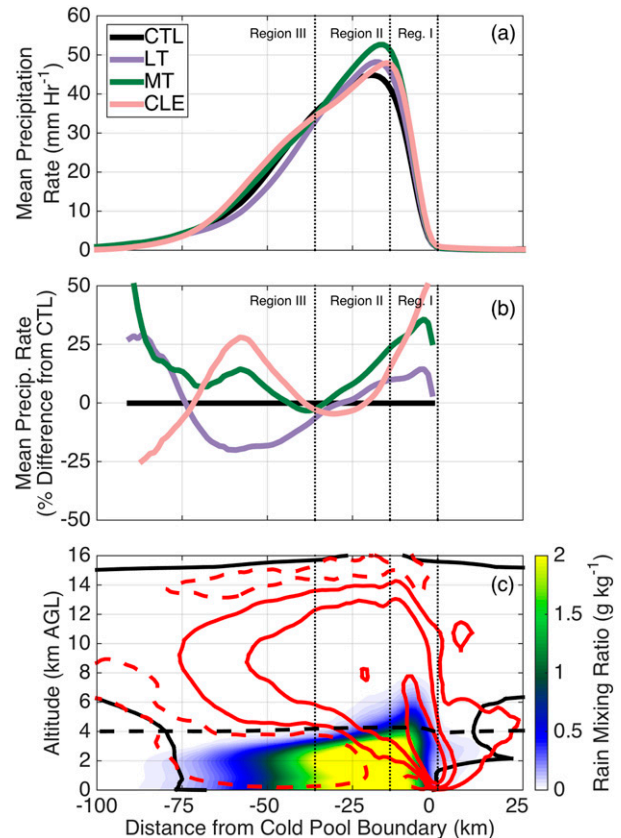


FIG. 6. (a),(b) Composite cross sections of surface hourly precipitation rates for the 24 May event simulations shown as (a) absolute values and (b) percentage difference from the CTL simulation. In (b), percentages are only shown where composite precipitation rates are greater than  $1 \text{ mm h}^{-1}$ . (c) Composite cross section from the 24 May CTL simulation of rain mixing ratio (shaded;  $\text{g kg}^{-1}$ ), with contours of the  $0.1 \text{ g kg}^{-1}$  total condensate mixing ratio (solid black line);  $0.25$ ,  $1.0$ , and  $3.0 \text{ m s}^{-1}$  updrafts (solid red lines);  $0.1 \text{ m s}^{-1}$  downdrafts (dashed red line); and the  $0^\circ\text{C}$  temperature level (dashed black line). The vertical dotted black lines partition the MCS cross section into precipitation regions (regions I, II, and III) based on different dominant precipitation pathways, which are discussed in the main text. Note that the horizontal axis represents the distance in kilometers from the leading cold pool boundary.

vertically integrated and compared (Fig. 7). Recall that within the first  $\sim 15$  km behind the leading cold pool boundary (region I), the MT and CLE precipitation rates had similar enhancements (Figs. 6a,b). With fewer APs in the lower troposphere in these simulations (see Fig. 4a), fewer cloud droplets were activated, and with less competition for water vapor, these cloud droplets grew faster from condensation to larger sizes, which created higher collision efficiencies and increased drizzle and rain production. This more efficient conversion of cloud mass to rain mass (i.e., warm-rain process) in regions with lower AP concentrations has been reported

TABLE 1. Mean precipitation rates for the 24 May event simulations within regions I, II, and III and for the entire cross section, as depicted in Fig. 6. The CTL values represent absolute precipitation rates ( $\text{mm h}^{-1}$ ), while the values for the other simulations represent percentage differences from the CTL simulation.

	Region			Total cross section
	I	II	III	
CTL ( $\text{mm h}^{-1}$ )	21.3	41.7	10.6	18.5
Percentage difference from the CTL simulation				
LT (%)	10.7	2.2	-12.4	-1.5
MT (%)	27.2	8.6	5.4	10.7
CLE (%)	24.4	-1.1	8.6	7.0

in numerous studies (e.g., Albrecht 1989). Figures 7a and 7b demonstrate that this warm-rain process was largely responsible for the enhanced precipitation near the leading cold pool boundary in the MT and CLE simulations, with, on average, 40%–50% higher conversion rates of cloud to rain within region I. While some fraction of this rain precipitates before reaching the freezing level, some rain is lofted above the freezing level within region I and enhances ice growth and precipitation processes in region I of the CLE and MT simulations (Figs. 7d,h). In the LT and CTL simulations, warm-rain processes were not only weaker in magnitude than the CLE and MT simulations, but the peak warm-rain conversions rates were also shifted several kilometers rearward because of the increased time needed to form rain within the front-to-rear storm-relative airflow in the propagating MCS.

Within the region between  $\sim 15$  and 35 km behind the leading cold pool boundary (region II), the melting of ice hydrometeors contributed a larger source of rain mass (Fig. 7c) than the conversion of cloud mass to rain mass (Fig. 7a), implying that precipitation in this region can be largely attributed to precipitation processes within the mixed-phase convective updrafts. Therefore, to further explore the impacts of the AP vertical location on precipitation within this region, vertical profiles of cloud and rain properties and processes within convective updrafts are shown in Fig. 8. For this analysis, convective updrafts were defined as regions where the vertical velocity was greater than  $5 \text{ m s}^{-1}$ , although the trends were largely insensitive to a range of the vertical velocity thresholds (e.g.,  $2\text{--}15 \text{ m s}^{-1}$ ). Within  $\sim 0\text{--}3 \text{ km}$  AGL, the trends in cloud water and rain properties (Figs. 8a–d) follow the changes in warm-rain processes, as explained above. With fewer lower-tropospheric APs in the MT and CLE simulations, there were also fewer cloud droplets, allowing them to grow to larger sizes and to be more efficiently converted to rain. However, above  $\sim 4 \text{ km}$  AGL, cloud droplet number mixing ratio (CDNMR) slightly

increased with height in the MT simulation but decreased in height in the other three simulations (Fig. 8b). This finding suggests that midtropospheric APs can become entrained within strong convective updrafts and initiate secondary nucleation of cloud droplets in the midtropospheric levels of these convective updrafts, as was shown in F04. Despite the presence of some pathways for midtropospheric APs to become entrained within convective updrafts, the MT CDNMR in the middle and upper troposphere were still lower than the CDNMR in the CTL and LT simulations. The midtropospheric source of aerosol in the MT simulation did, however, result in higher CDNMR than in the CLE simulation.

Although CDNMR is higher between 4 and 6 km AGL (Fig. 8b) in the LT and CTL simulations, moderate cloud mixing ratios of  $\sim 1.5 \text{ g kg}^{-1}$  resulted in mean cloud droplet diameters that were greater than  $20 \mu\text{m}$  within the mixed-phase updrafts (Fig. 8c). The collection efficiency between cloud droplets and ice hydrometeors decreases significantly as cloud droplet diameters decrease below  $20 \mu\text{m}$  and remains approximately constant above  $20 \mu\text{m}$  (Saleeby and Cotton 2008). Therefore, the CTL and LT simulations had enhanced cloud droplet riming rates when compared to the MT and CLE simulations because of increased cloud droplet number concentrations and the relatively small changes in the collection efficiency. This balance between mean cloud droplet diameter and cloud droplet number in terms of cloud droplet riming efficiency is discussed in detail in Saleeby et al. (2016).

However, in terms of the overall impact of the vertical location of aerosol particles on mixed-phase precipitation processes, the decreases in cloud riming in the CLE and MT simulations were partially offset because of increases in accretion of rain by ice hydrometeors (Fig. 8f). Higher concentrations of raindrops that were formed via warm-rain processes in the CLE and MT simulations were lofted into the MCS mixed-phase region to drive this trend. This intensification of rain accretion by ice hydrometeors along with the riming of newly activated cloud droplets in the mixed-phase region contributed to the MT simulation having the most intense precipitation within the region between  $\sim 15$  and 35 km behind the leading cold pool boundary (region II). These trends in mixed-phase precipitation processes among the sensitivity simulations are also apparent in Figs. 7e–h (region II).

The precipitation within the stratiform region of MCSs is largely associated with hydrometeors that are advected rearward from the mid- and upper-tropospheric levels of convective updrafts (e.g., Smull and Houze 1985; Rutledge and Houze 1987). The LT and CTL simulations, which had higher CDNMR and cloud riming rates within

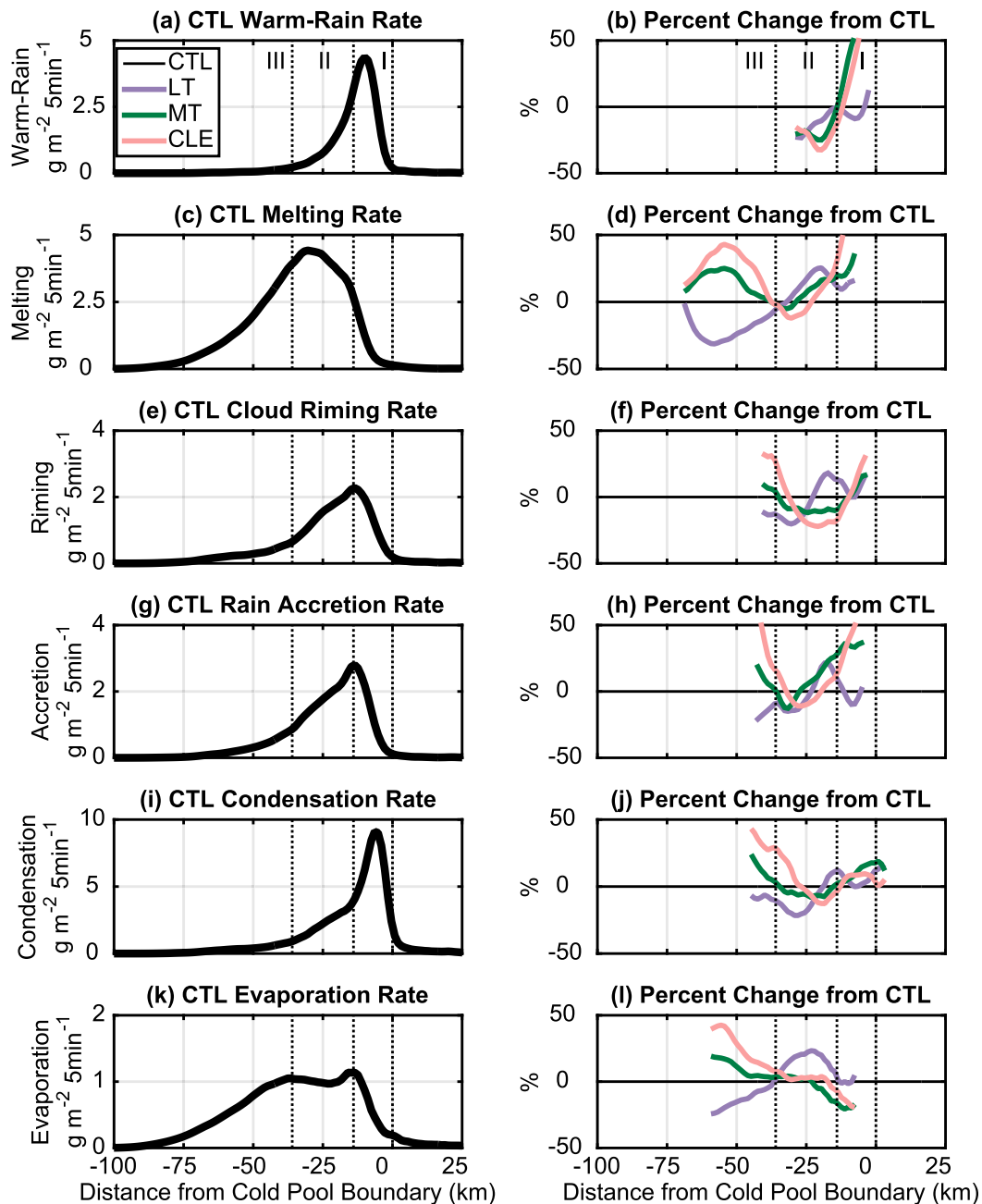


FIG. 7. Composite cross sections of vertically integrated microphysical process rates from the 24 May simulations. (left) Values for the CTL simulation and (right) percentage changes from the CTL case. Percentage changes are only shown where the vertically integrated process rate is greater than  $0.5 \text{ g m}^{-2} (5 \text{ min})^{-1}$ . Microphysical processes shown are (a),(b) cloud-to-rain conversion, (c),(d) melting of ice hydrometeors, (e),(f) riming of cloud water by ice, (g),(h) accretion of rain by ice, (i),(j) condensation of vapor onto liquid hydrometeors, and (k),(l) evaporation of vapor from liquid hydrometeors. The vertical dotted black lines partition the MCS cross section into precipitation regions (regions I, II, and III) based on different dominant precipitation pathways, which are discussed in the main text.

the convective updrafts (Figs. 8b,e), had lower cloud mixing ratios in the upper portions of the convective updrafts as a result of the enhanced cloud droplet riming (Fig. 8a). In the LT and CTL simulations, this

enhancement of mixed-phase ice growth created both larger ice hydrometeors (e.g., hail) that sedimented more quickly near the convective updrafts (region II) and also became a sink of cloud droplets that would have

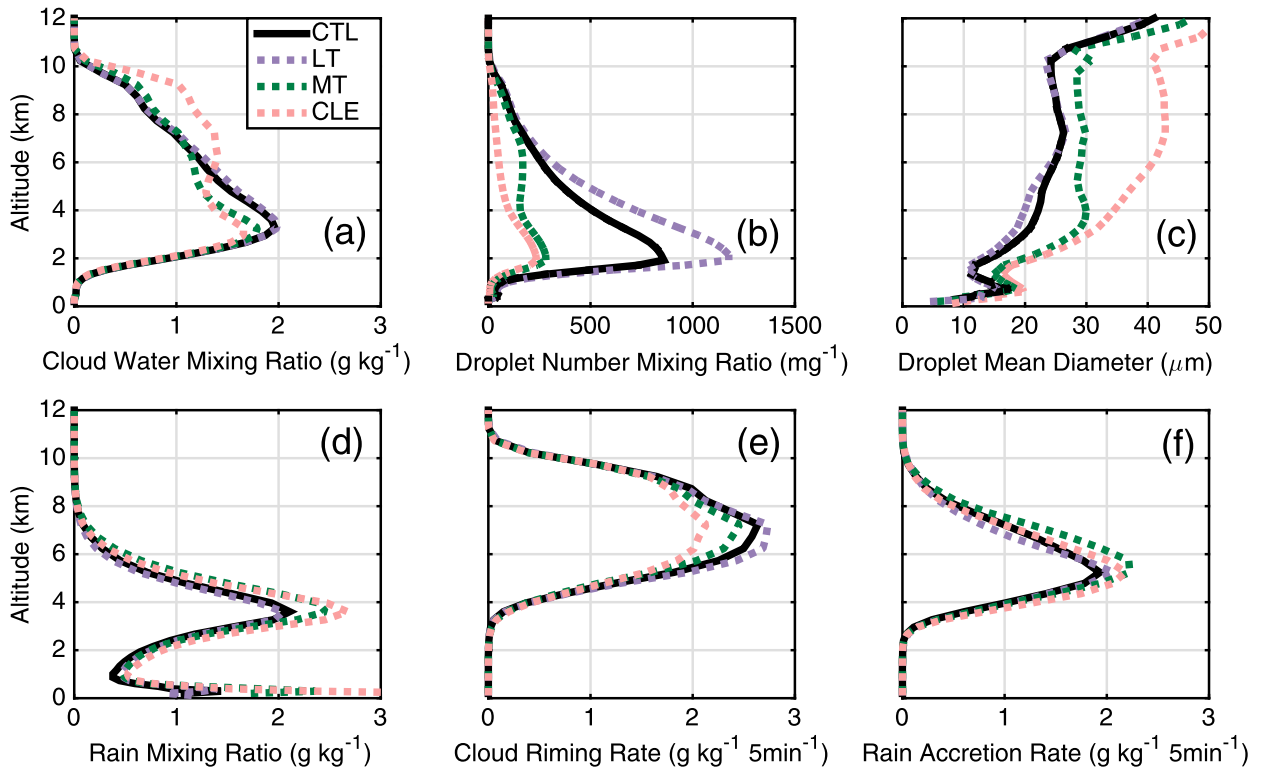


FIG. 8. Vertical profiles of (a) cloud water mixing ratio, (b) CDNMR, (c) mean cloud droplet diameter, (d) rain mixing ratio, (e) the riming rate of cloud water by ice, and (f) the accretion rate of rain by ice within the convective updrafts for the 24 May event simulations. Quantities were averaged over all grid points where the vertical velocity was greater than  $5 \text{ m s}^{-1}$  at each model level in order to represent averages only over convective updrafts.

otherwise been advected by the front-to-rear ascending flow of the MCS into the upper and rearward regions of the MCS. The combination of these processes resulted in a decrease in hydrometeors and precipitation processes farther rearward ( $\sim 35\text{--}100 \text{ km}$  behind the leading cold pool boundary; region III) in the LT and CTL simulations (Fig. 7). Composite cross sections of total condensate mixing ratio for the suite of simulations (Fig. 9) further support this hypothesis. The MT and CLE simulations, which had lower cloud riming rates (Figs. 7 and 8), also had lower total condensate amounts in the region collocated and rearward of the mixed-phase convective updrafts (Figs. 9c,d, region II). In the MT and CLE simulations, more cloud water was transported to the upper and rearward portions of the MCS, enhancing total condensate and precipitation within the MCS stratiform region (region III).

#### 4. Comparison to MCS event on 20 May 2011

##### a. Precipitation cross section

Figures 10–12 are similar to Figs. 6–8 but represent the results for the 20 May event simulations. A comparison

of the cross sections of precipitation rates and MCS structure from the 20 May event (Fig. 10) to the 24 May event (Fig. 6) highlights several differences between these two LLTS MCS events. The 20 May simulated MCS had a precipitation region that was approximately double the size of the 24 May MCS, which is related to the more rearward tilt of the convective updrafts in the 20 May MCS. The contour of  $1.0 \text{ m s}^{-1}$  vertical motion reaches its maximum altitude at  $\sim 40 \text{ km}$  behind the leading cold pool boundary in the 20 May CTL simulation (Fig. 10c) versus  $\sim 15 \text{ km}$  behind the leading cold pool boundary in the 24 May CTL simulation (Fig. 6c). Also, the 20 May convective precipitation rates were not as intense as the 24 May event, with peak cross-sectional precipitation rates that were 30%–45% lower than the 24 May event.

In terms of precipitation rate trends among the 20 May sensitivity simulations, within the first  $\sim 15 \text{ km}$  behind the leading cold pool boundary, MT and CLE simulations both had an average increase in precipitation rates of  $\sim 20\%$  over CTL, with this region accounting for  $\sim 20\%$ – $25\%$  of the total precipitation, both of which were consistent with the results from the 24 May simulations. However, in the 20 May event, the

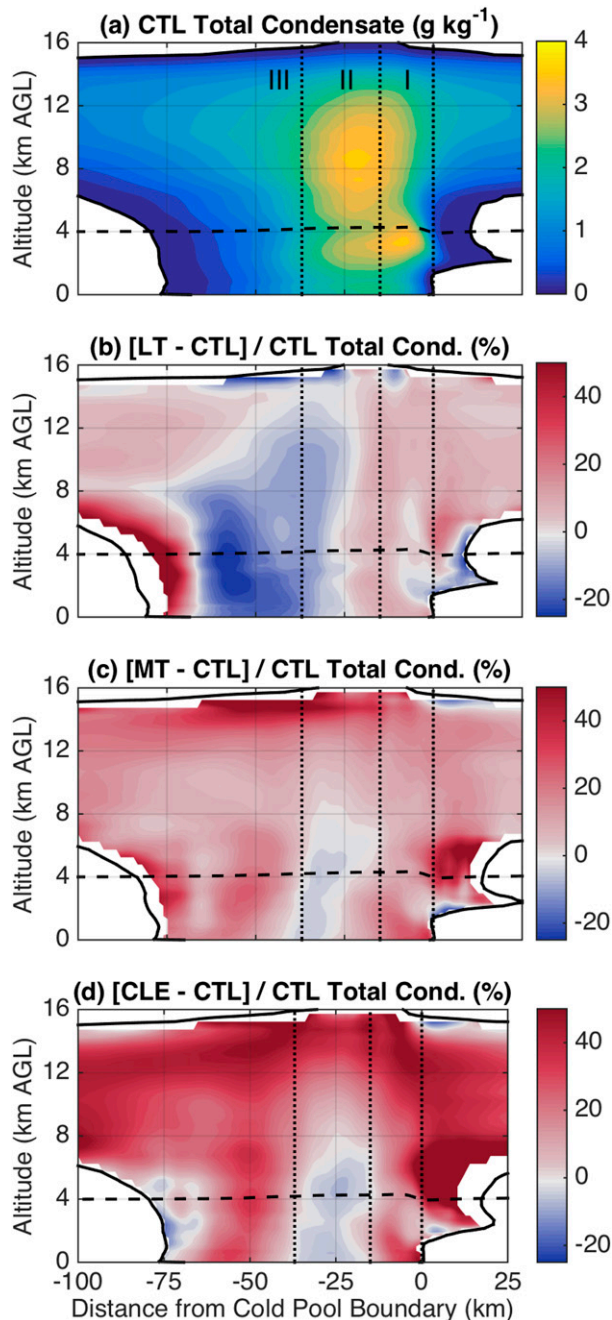


FIG. 9. Composite cross sections of total condensate mixing ratio for the 24 May simulations. (a) Absolute total condensate values ( $\text{g kg}^{-1}$ ) for CTL and (b)–(d) percentage differences in total condensate from CTL for LT, MT, and CLE, respectively. The black solid contour represents the  $0.1 \text{ g kg}^{-1}$  total condensate mixing ratio, and the black dashed contour represents the  $0^\circ\text{C}$  temperature level. The vertical dotted black lines partition the MCS cross section into precipitation regions (regions I, II, and III) based on different dominant precipitation pathways, which are discussed in the main text.

MT total cross-sectional precipitation was within 2% of the CTL and LT simulations, which all had  $\sim 8\%$  more surface precipitation than the CLE simulation. Recall, in the 24 May event, the MT total cross-sectional precipitation amount was more similar to the CLE simulation.

### b. Microphysical processes

To explain these precipitation trends and to better compare them to the 24 May simulations, similar vertically integrated microphysical process rates of composite cross sections and vertical profiles within convective updrafts are shown in Figs. 11 and 12, respectively. Similar to the 24 May event, there was an enhancement of precipitation in the MT and CLE simulations in the first  $\sim 15 \text{ km}$  behind the leading cold pool boundary (Figs. 10a,b), which can be largely attributed to enhanced warm-rain processes (Figs. 11a,b) and subsequent increases in ice precipitation processes in this region (Figs. 11c–h), as some of this rain was lofted above the freezing level. However, in the region collocated and rearward of the mixed-phase convective updrafts ( $\sim 25\text{--}65 \text{ km}$  behind the leading cold pool boundary; Fig. 10c), the vertically integrated microphysical process rates in the MT simulation were more similar to the CTL and LT simulations (Fig. 11, right column). Recall that in region II of the 24 May simulations, the MT simulation had many microphysical process rate trends that were similar to the CLE simulation (Fig. 7, right column).

Above  $\sim 4 \text{ km}$  AGL in the MT convective updrafts, there was an increase in CDNMR with altitude (Fig. 12b), while the other simulations all had decreasing CDNMR with height. This increase in CDNMR with altitude in the MT simulation, which was representative of midtropospheric APs being activated into cloud droplets within the mixed-phase cloud region, was consistent with the 24 May simulations (Fig. 8b), although it was more pronounced in the 20 May simulations. In the 20 May simulations, the MT CDNMR surpassed the LT and CTL CDNMR above  $6 \text{ km}$  AGL with  $40\%\text{--}80\%$  greater CDNMR between  $6$  and  $9 \text{ km}$  AGL (Fig. 12b). This increase in CDNMR within the mixed-phase convective updrafts in the MT simulation, along with sizeable cloud water mixing ratios that resulted in mean cloud droplet diameters of  $20\text{--}30 \mu\text{m}$ , enhanced cloud-riming rates such that they were within  $5\%$  of the LT and CTL simulation riming rates between  $5$  and  $9 \text{ km}$  AGL (Fig. 12e), as opposed to  $\sim 10\%$  lower, as they were in 24 May simulations (Fig. 8e).

More rain accretion by ice hydrometeors in the mixed-phase convective updrafts acted to balance lower cloud riming rates in the CLE and MT simulations in the

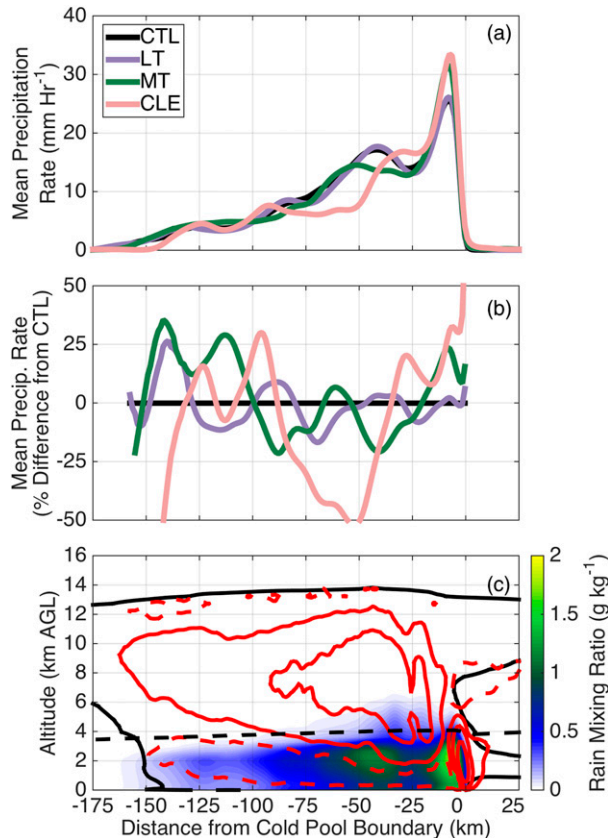


FIG. 10. (a),(b) Composite cross sections of surface hourly precipitation rates for the 20 May event simulations shown as (a) absolute values and (b) percentage difference from the CTL simulation. In (b), percentages are only shown where composite precipitation rates are greater than  $1 \text{ mm h}^{-1}$ . (c) Composite cross section from the 20 May CTL simulation of rain mixing ratio (shaded;  $\text{g kg}^{-1}$ ), with contours of the  $0.1 \text{ g kg}^{-1}$  total condensate mixing ratio (solid black line);  $0.25$ ,  $1.0$ , and  $3.0 \text{ m s}^{-1}$  updrafts (solid red lines);  $0.1 \text{ m s}^{-1}$  downdrafts (dashed red line); and the  $0^\circ\text{C}$  temperature level (dashed black line). Note that the horizontal axis represents the distance in kilometers from the leading cold pool boundary.

24 May simulations (Figs. 8e,f). However, rain accretion played a weaker role in the enhancement of mixed-phase convective precipitation in the 20 May simulations (cf. Fig. 12f with Fig. 8f), which was due to weaker updrafts below the freezing level and, thus, a larger proportion of rain precipitating to the surface before being lofted upward into the mixed-phase region of the convective updrafts (cf. Fig. 10c with Fig. 6c). Therefore, cloud droplet riming accounted for a high fraction of the mixed-phase precipitation formation within convective updrafts in the 20 May simulations.

Changes to precipitation processes and hydrometeor characteristics can alter the cold pool characteristics, which then can have significant dynamical feedbacks within MCSs (Tao et al. 2007; Seigel et al. 2013; Lebo

and Morrison 2014). Figure 13 shows composite cross sections of density potential temperature  $\theta_p$  within the lowest 4 km AGL and vertical motions for the LT, MT, and CLE simulations as differences from the CTL simulation for the 20 May event. The CLE simulation had surface  $\theta_p$  perturbations greater than  $+0.5 \text{ K}$  throughout the majority of the MCS cross section, while the LT and MT simulations had  $\theta_p$  values that were generally within  $0.25 \text{ K}$  of CTL throughout the entire cold pool. The weaker cold pool in the CLE simulation was associated with lower evaporation rates from 30 to 90 km behind the leading cold pool boundary (Figs. 11k,l). Although raindrops were smaller in size within this region of the CLE simulation, fewer raindrops and less total rain mass resulted in the lower evaporation rates.

Warmer cold pools propagate at slower speeds as they have weaker temperature gradients across the cold pool boundary and, therefore, weaker pressure gradients that drive the cold pool boundary propagation (Benjamin 1968). As such, the CLE cold pool boundary propagated at slower speeds (not shown). With faster system propagation in association with colder cold pools, the front-to-rear storm-relative flow was more intense in the CTL, LT, and MT simulations as compared to the CLE simulation. Updrafts that were more erect throughout the depth of the cloud system in CLE are further evidence of this. Figures 13e–h demonstrate that the CLE convective updraft velocities were more intense closer to the leading cold pool boundary, indicating more upright convection along the leading line. This explanation is consistent with RKW theory, which states that an optimal balance between the environmental shear and the cold pool circulation produces the strongest lift and the most upright convection (Rotunno et al. 1988; Bryan et al. 2006). More intense cold pools and faster cold pool propagation speeds in CTL, MT, and LT also enhanced rearward transport of both vertical momentum and water within the MCS and can assist in explaining the large differences and shifts in precipitation processes between the CLE and MT, LT, and CTL simulations seen in Fig. 11. Such aerosol-induced differences in cold pool strength and the resulting dynamic feedback on the MCS precipitation structure were not evident in the 24 May simulations, which is likely due to differences in the nonlinear interactions between precipitation, cold pool characteristics, environmental characteristics, and MCS structure.

The results from the simulations presented here of two MCS events suggest that aerosol–precipitation interactions within LLTS MCSs may be best understood by assessing changes to microphysical processes along the front-to-rear, ascending flow and within MCS regions that are dominated by distinct microphysical

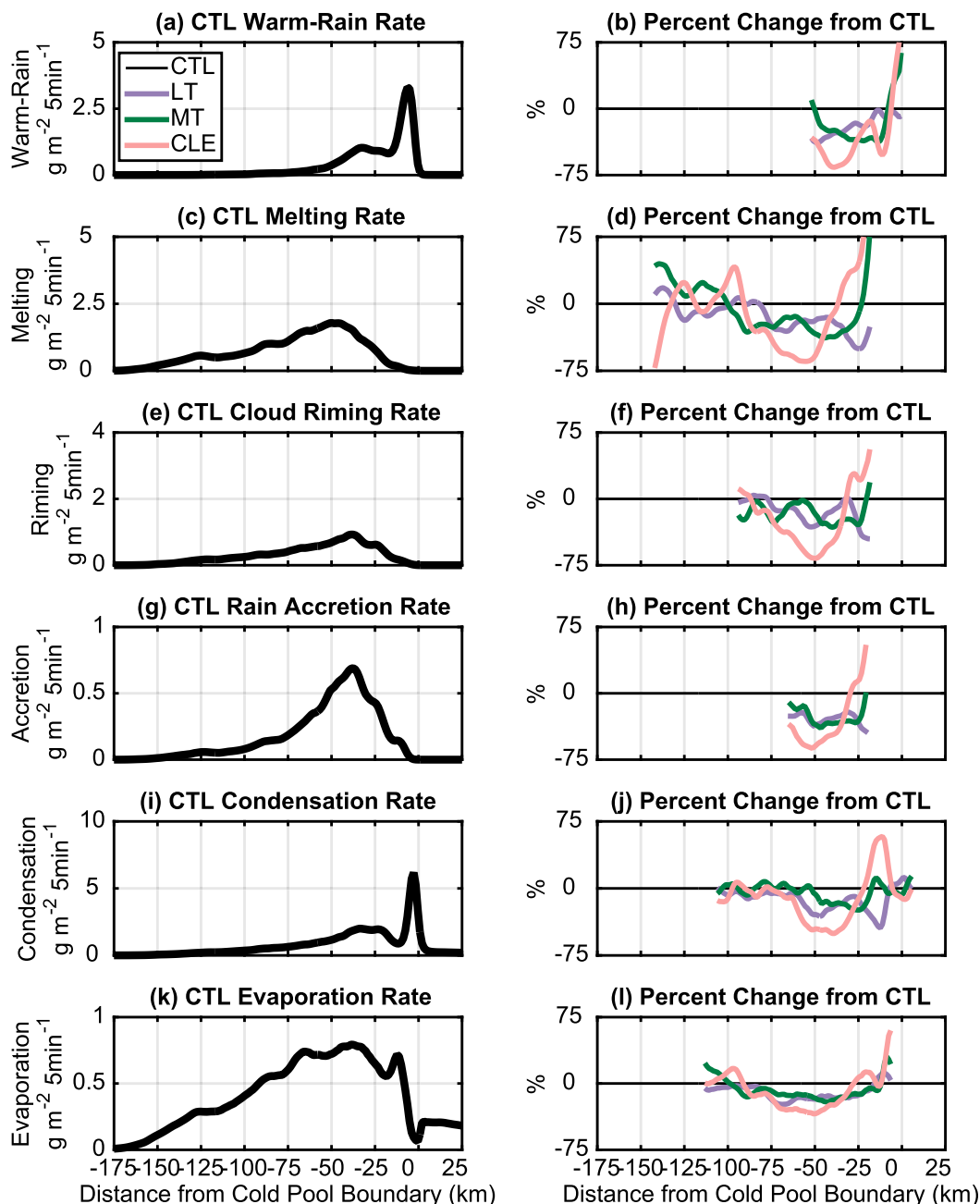


FIG. 11. Composite cross sections of vertically integrated microphysical process rates from the 20 May simulations. (left) Values for the CTL simulation and (right) percentage changes from the CTL case. Percentage changes are only shown where the vertically integrated process rate is greater than  $0.3 \text{ g m}^{-2} (5 \text{ min}^{-1})$ . Microphysical processes shown are (a),(b) cloud-to-rain conversion, (c),(d) melting of ice hydrometeors, (e),(f) riming of cloud water by ice, (g),(h) accretion of rain by ice, (i),(j) condensation of vapor onto liquid hydrometeors, and (k),(l) evaporation of vapor from liquid hydrometeors.

processes. Figure 14 shows an LLTS MCS cross-sectional schematic that will assist in summarizing the microphysical MCS precipitation pathways discussed in this study. The three regions in Fig. 14 represent regions of the MCS that are dominated by different microphysical

processes and are slanted to account for the fall trajectories of hydrometeors associated with a propagating MCS. Within region I in Fig. 14, lower-tropospheric APs influence the precipitation amounts via warm-rain processes, with higher concentrations of APs suppressing

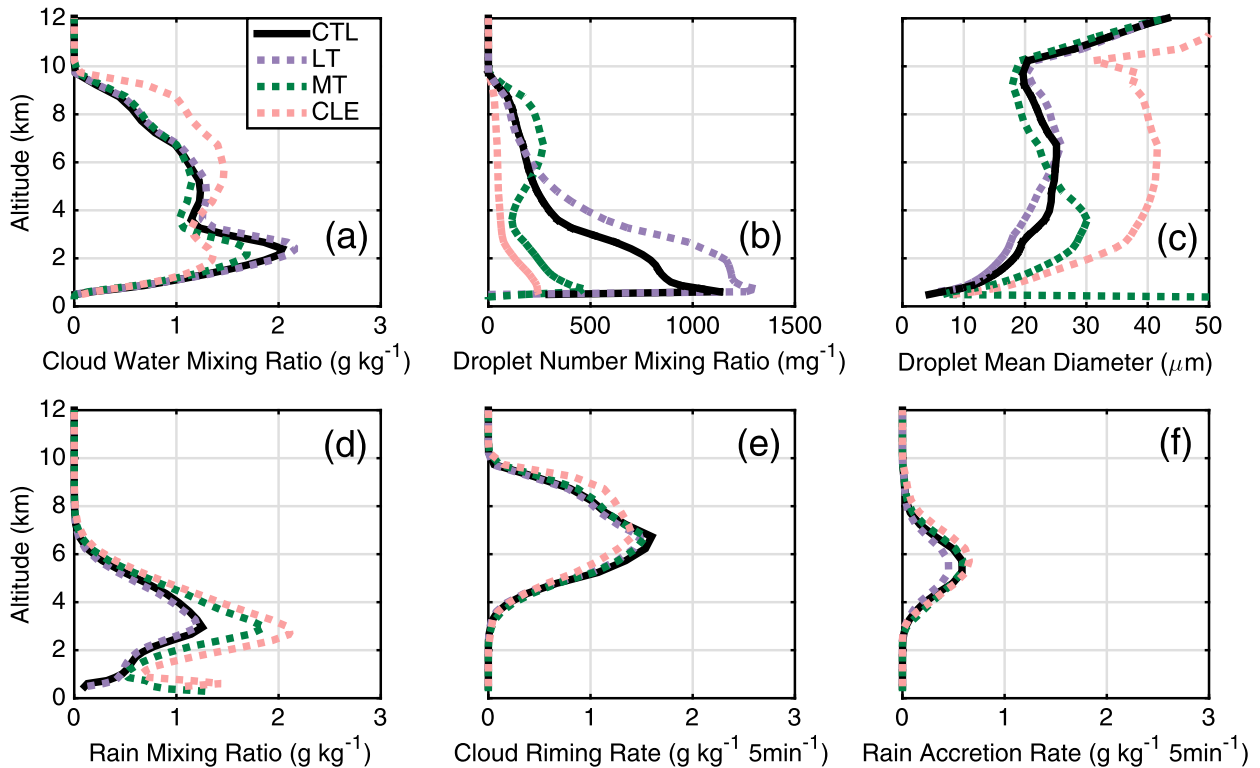


FIG. 12. Vertical profiles of (a) cloud water mixing ratio, (b) CDNMR, (c) mean cloud droplet diameter, (d) rain mixing ratio, (e) the riming rate of cloud water by ice, and (f) the accretion rate of rain by ice within the convective updrafts for the 20 May event simulations. Quantities were averaged over all grid points where the vertical velocity was greater than  $5 \text{ m s}^{-1}$  at each model level in order to represent averages only over convective updrafts.

precipitation rates. This aerosol–precipitation effect was consistent in both the 20 and 24 May events, and precipitation within this region contributed  $\sim 20\%$  of the total cross-sectional precipitation. Precipitation processes occurring within the mixed-phase region of the convective updrafts predominated rain amounts within region II, which accounted for the majority of surface precipitation in both MCS events. Midtropospheric APs can become entrained within the mixed-phase region, thus enhancing cloud droplet number concentrations and ice growth via riming, although the amount of APs mixing into convective updrafts in the middle troposphere varied between the two MCS events presented in this study. Furthermore, rain and cloud that were formed in region I can be lofted into region II within the front-to-rear ascending flow and assist in ice growth via cloud riming and rain accretion by ice hydrometeors. Sedimenting precipitation and enhanced collisional processes (i.e., cloud riming) within region II can create a sink of hydrometeor mass that would otherwise be advected into region III. This advection of hydrometeors, vapor, and momentum in the front-to-rear ascending flow generated precipitation within region III (the

stratiform region) and, therefore, is dependent on the processes occurring in regions I and II.

### 5. Environmental modulation of aerosol–precipitation interactions

The LLTS MCS schematic in Fig. 14 can also be useful in demonstrating why the simulations of the two MCS events resulted in different precipitation responses from midtropospheric APs. Recall, in the 24 May simulations, the MT and CLE simulations both had  $\sim 10\%$  increases in the total cross-sectional surface precipitation over the CTL and LT simulations, implying that lower-tropospheric APs played a more important role than midtropospheric APs on the overall precipitation response. However, in the 20 May simulations, the MT simulation was more in keeping with the LT and CTL simulations, suggesting a larger impact from midtropospheric APs in the 20 May event. In the 24 May simulations, more intense updrafts were present, and therefore, a larger proportion of rain hydrometeors were vertically advected from region I into region II, as opposed to precipitating from the system before

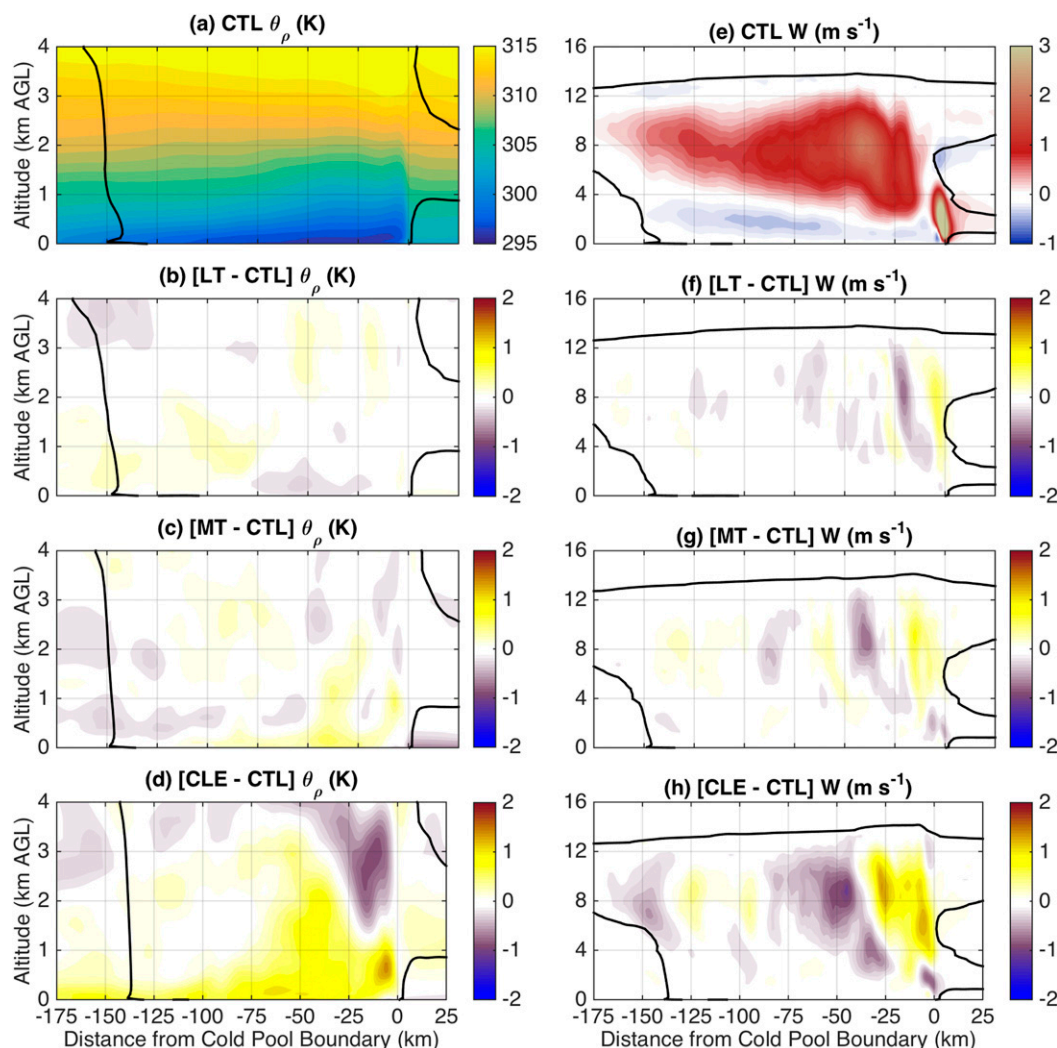


FIG. 13. Composite cross sections of density potential temperature  $\theta_p$  (K) and vertical velocity  $W$  ( $\text{m s}^{-1}$ ) for the 20 May simulations. (a)  $\theta_p$  for CTL and (b)–(d) differences in  $\theta_p$  from CTL for LT, MT, and CLE, respectively. The black contour represents the  $0.1 \text{ g kg}^{-1}$  total condensate mixing ratio. (e)–(h) As in (a)–(d), respectively, but for  $W$  ( $\text{m s}^{-1}$ ). Note the difference in the vertical-axis scales between the columns.

reaching the mixed-phase convective updrafts. This can be seen by comparing the MCS structure from the two events in Figs. 6c and 10c. As such, in the 24 May simulations, the lower-tropospheric AP response in region I became more relevant to mixed-phase precipitation processes. Furthermore, the more upright and intense convective updrafts in the 24 May simulations may be more impenetrable to midtropospheric entrainment, thus lowering the amount of environmental midtropospheric APs that can impact the mixed-phase region of the MCS (McGee and van den Heever 2014). In these simulations, this was evident by fewer cloud droplets in the midtropospheric convective updrafts of the MT 24 May simulation (Fig. 8b) as compared to the MT

20 May simulation (Fig. 12b). This difference in the convective updraft structure between these two MCS events can be largely explained by variations in how the two MCSs interacted with their respective environments.

Figure 15 presents skew  $T$ - $\log p$  diagrams of the environmental conditions ahead of both MCS events for the MT simulations, as well as plan views of horizontal wind and equivalent potential temperature at  $\sim 1.5 \text{ km AGL}$ . The skew  $T$ - $\log p$  diagrams were calculated from composite cross sections, where the vertical profiles of atmospheric variables were averaged between 20 and 50 km ahead of the MCS leading cold pool boundary. There are a number of differences in these

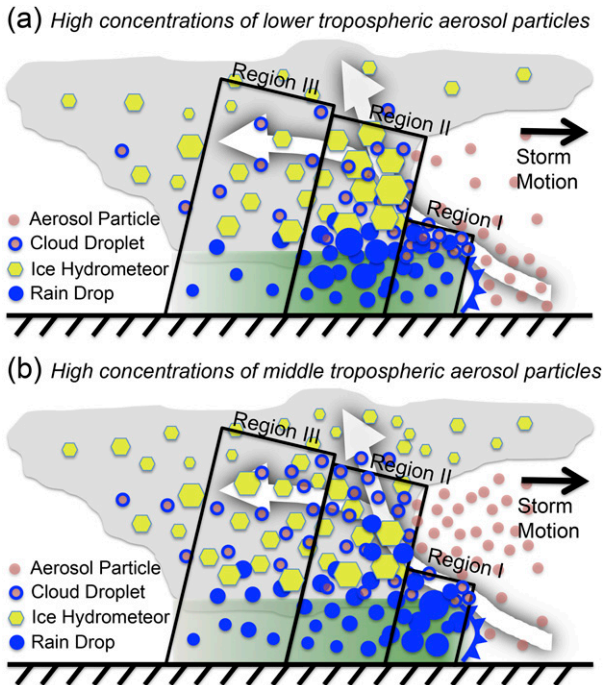


FIG. 14. Schematic of an LLTS MCS under high concentrations of (a) LT and (b) MT APs. The gray area represents cloudy regions, while the green shading represents rainfall with darker shading depicting heavier rain. The blue frontal symbols represent the leading cold pool boundary, and the white arrows represent the primary front-to-rear ascending flow. The three boxes represent three different precipitation regions of the MCS where different microphysical processes are governing the precipitation. Particle types are specified in the legends, with the amounts and sizes of hydrometeors representative of the relative concentrations and mean diameters of particles within those regions.

thermodynamic diagrams, including differences in atmospheric moisture and boundary layer depth. However, the difference that may be most significant in regulating the relative roles of lower- and midtropospheric APs in MCS precipitation is the difference in line-normal wind shear, which plays a crucial role in determining MCS structure (e.g., Rotunno et al. 1988; Bryan et al. 2006). While both environments were associated with veering wind profiles through the lower and middle troposphere (Figs. 15a,c), the horizontal orientation of the MCSs altered the relative amount of shear perpendicular to the leading convective line (line normal). The 20 May MCS was aligned in the north-south direction, approximately parallel to the lower-tropospheric environmental wind vectors ahead of the leading cold pool boundary (Fig. 13b). Alternatively, the 24 May MCS was oriented along a northeast-southwest axis (Fig. 13d), thus having a larger component of the environmental wind ahead of the leading cold pool boundary perpendicular to this axis. The MCS alignment

created lower storm-relative environmental wind shear in the 20 May MCS simulations. For example, the low-level line-normal wind shear was  $\sim 8 \text{ m s}^{-1}$  in the 20 May simulation versus  $\sim 16 \text{ m s}^{-1}$  in the 24 May simulation, based on the soundings in Fig. 15. Low-level wind shear was calculated as the minimum line-normal wind speed in the lowest 1 km AGL subtracted from the line-normal wind speed at 3 km AGL. In situations where the cold pools have similar intensities and structures, lower environmental wind shear can lead to a more rearward-tilted updraft, as the circulation associated with the cold pool overpowers the wind shear (e.g., Rotunno et al. 1988; Bryan et al. 2006). The structure of the 20 May MCS (Fig. 10c) more closely resembles the idealized simulations in low-wind-shear conditions completed by Lebo and Morrison (2014, their Fig. 4), providing further evidence that this lack of environmental line-normal wind shear is driving the structural differences between these two simulated MCS events.

These simulations demonstrate that in stronger line-normal wind shear conditions, which created more upright and intense updrafts (i.e., the 24 May event), perturbations of lower-tropospheric APs played a more significant role in altering MCS precipitation than perturbations of midtropospheric APs. This was due to both enhanced vertical advection of hydrometeors to the mixed-phase region that originally formed on lower-tropospheric APs near the leading cold pool boundary and the barriers to midtropospheric environmental air mixing into the intense, upright convective updrafts. In weaker line-normal wind shear conditions (i.e., the 20 May event), which created a more rearward-tilting MCS structure, both of these key effects acting in the stronger line-normal wind shear conditions are reduced, and therefore, midtropospheric APs can have a more significant impact on MCS precipitation. Last, it is important to note that dynamic feedbacks, such as changes to cold pools, within these systems can also alter the structure and, thus, aerosol-precipitation interactions within MCSs, as was the case in the CLE 20 May simulation, thus further complicating the microphysical role of aerosol particles on MCS precipitation.

## 6. Sensitivity to grid resolution

Several studies have shown, using idealized simulations of squall lines, that the amount of environmental air mixed into the leading convective line updrafts is dependent on the simulation grid spacing (Bryan et al. 2003; Lebo and Morrison 2015). Lebo and Morrison (2015) reported a large shift in convective updraft characteristics when the horizontal grid spacing was decreased from 500 to 250 m, suggesting a regime shift

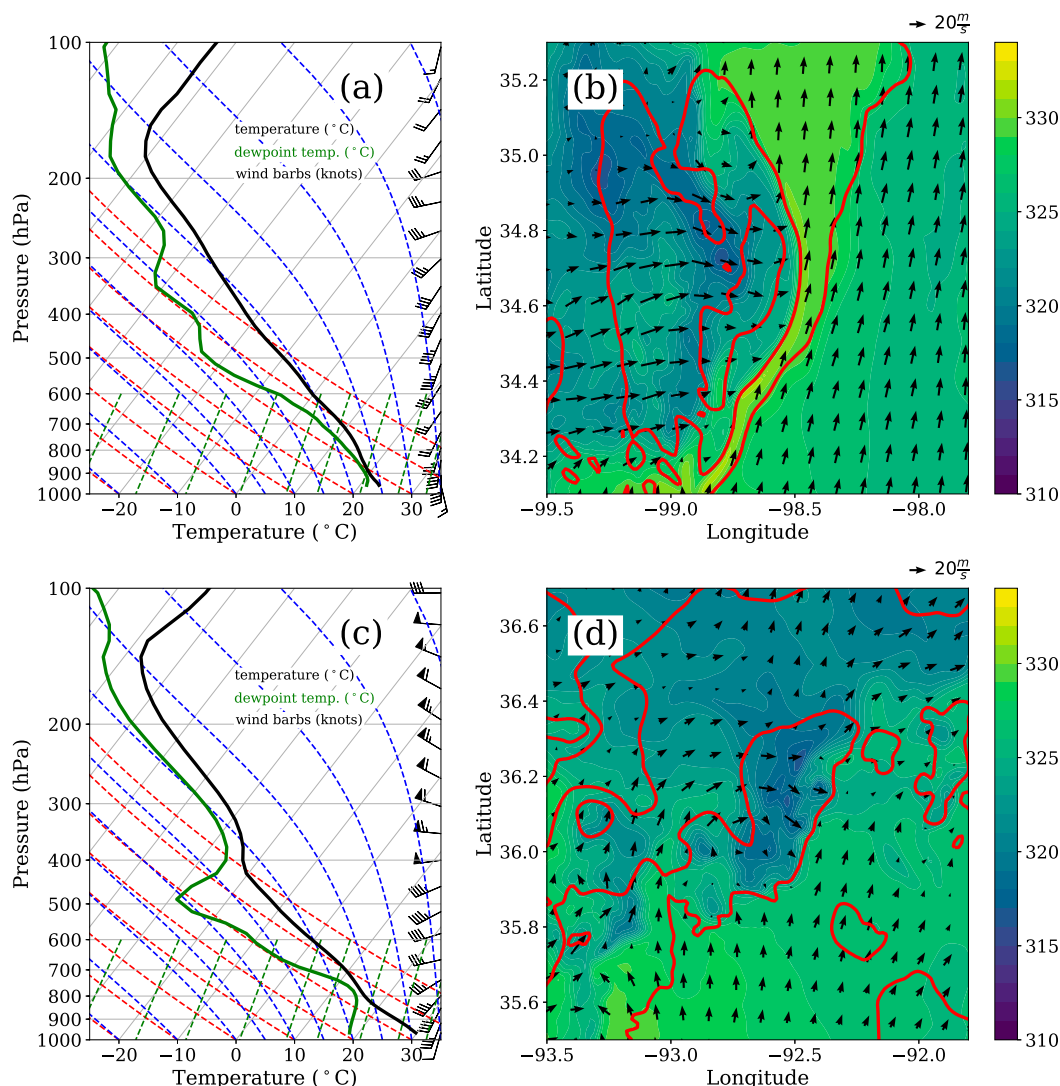


FIG. 15. (a),(b) Environmental conditions associated with the 20 May simulations at 0800 UTC. (a) A skew  $T$ - $\log p$  diagram from the region ahead of the leading cold pool boundary and (b) a plan view of surface equivalent potential temperature  $\theta_e$  (shaded), surface winds (arrows), and vertically integrated condensate of 8 mm (red contour). Data shown here are from the MT simulation. (c),(d) As in (a) and (b), respectively, but for the 24 May MT simulation at 0200 UTC.

from more laminar to turbulent flows when moving toward large-eddy-simulation scales. To assess the grid-spacing dependence of the relative mixing of mid-tropospheric aerosol particles into strong convective updrafts, four additional simulations (MT and LT cases for both MCS events) were conducted at higher spatial resolution (300-m horizontal grid spacing), as explained in section 2a. The analysis methods for these higher-resolution simulations were the same as for the original simulations, as described in section 2c.

Figure 16 shows CDNMR within convective updrafts for both the original simulations and the high-resolution simulations. All higher-resolution simulations show

enhanced CDNMR in the middle troposphere, which is consistent with prior studies that predict enhanced mixing of midtropospheric air at finer grid spacing. However, critical to the goals of the research described here are the trends in convective updraft CDNMR between the LT and MT simulations and the trends between the 20 and 24 May MCS events, which are largely consistent across the original and high-resolution simulations. This suggests that the findings reported here for the impacts of environmental mixing in the simulations using 1.2-km horizontal grid spacing—namely, that 1) midtropospheric APs mix into convective updrafts and enhance cloud droplet number and

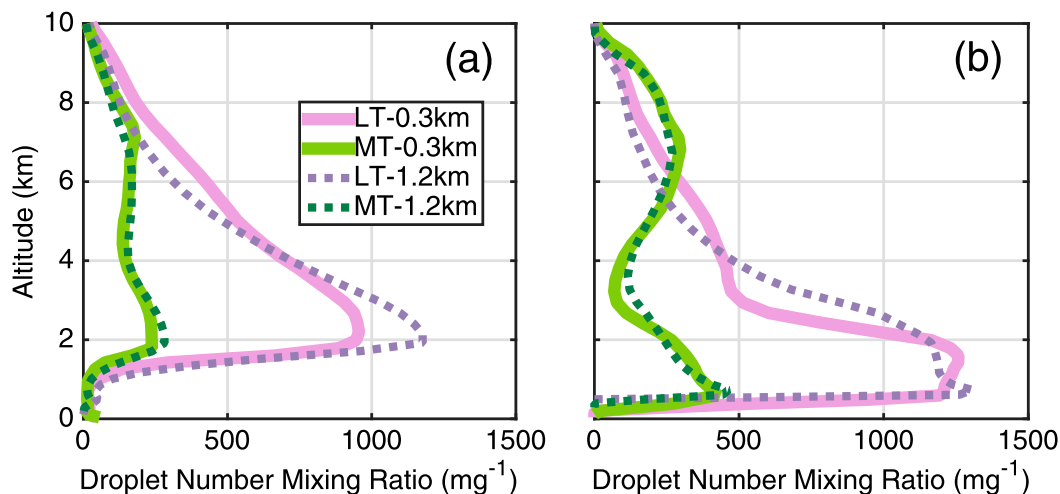


FIG. 16. Vertical profiles of CDNMR within the convective updrafts for the (a) 24 and (b) 20 May event simulations for both the original simulations (1.2-km horizontal grid spacing; dotted lines) and the high-resolution simulations (300-m horizontal grid spacing; solid lines). Quantities were averaged over all grid points where the vertical velocity was greater than  $5 \text{ m s}^{-1}$  at each model level in order to represent averages only over convective updrafts.

2) the 20 May event, which had weaker line-normal wind shear and a more rearward-tilted MCS structure, also had more mixing of midtropospheric aerosols into the convective updrafts—are also observed when using finer grid resolutions (300 m). This suggests a certain degree of robustness in these trends.

## 7. Conclusions

The goal of this study was to assess the relative roles of midtropospheric and lower-tropospheric aerosol particles (APs) in MCS precipitation during the mature storm stage. Two LLTS MCSs from the MC3E field campaign (20 and 24 May 2011) were simulated with the RAMS numerical model. These MC3E MCS events were especially relevant for this study since expansive biomass-burning events in Central America and Mexico occurred concurrently with MC3E, and biomass-burning APs from this region can be advected into the southern United States within both the lower and middle troposphere.

Meteorological reanalysis and aerosol data during MC3E were used to initialize the MCS simulations. For each MCS event, simulations were conducted with three different aerosol profiles in which the vertical location of the APs was varied while keeping the total vertically integrated AP mass (and number) constant. In this way, changes to MCS precipitation between the simulations could be more directly attributed to the vertical variations in AP concentrations, as opposed to the total amount of APs. Simulations were also initialized with a fourth, cleaner aerosol profile for comparison. Composite cross

sections relative to the propagating, leading cold pool boundary were used to quantify and understand changes in precipitation among the simulations, and a schematic of an LLTS MCS (Fig. 14) was used to assist in explaining the microphysical precipitation responses to the variations in AP concentrations.

Several aerosol-induced impacts on MCS precipitation were evident in both sets of simulations and, therefore, may also be applicable to other MCSs. It was found that lower-tropospheric APs had a consistent microphysical effect on precipitation directly behind the leading cold pool boundary for both simulated events (Fig. 14, region I). Fewer lower-tropospheric APs caused a  $\sim 20\%$  enhancement in precipitation rates in the first 15 km behind the leading cold boundary during the mature stage of the MCS events, which was primarily a result of more effective conversion from cloud to rain (warm-rain process). The precipitation associated with the mixed-phase region of convective updrafts (Fig. 14, region II) accounted for the majority of surface precipitation in the cross sections, and significant amounts of midtropospheric APs were entrained within the mixed-phase regions of the convective updrafts, thus increasing the number of cloud droplets and ice hydrometeor growth via cloud riming. However, hydrometeors that were transported from near the leading cold pool boundary (Fig. 14, region I) into the mixed-phase convective region also impacted precipitation processes in this zone (Fig. 14, region II). The relative impact of lower- versus midtropospheric APs on these mixed-phase precipitation processes varied between the two MCS events simulated and was highly dependent on the MCS structure. In stronger line-normal

wind shear conditions (i.e., the 24 May simulations), more upright and intense convective updrafts favored more lofting of hydrometeors near the cold pool boundary (Fig. 14, region I) into the mixed-phase convective updrafts (Fig. 14, region II). Also, fewer cloud droplets in the midtropospheric convective updrafts suggested less mixing of midtropospheric environmental air into the more intense updrafts that formed during the 24 May MCS. The formation of intense precipitation via both cloud riming and rain accretion by ice hydrometeors within region II created a sink of hydrometeors via precipitation that would otherwise be advected rearward into the trailing stratiform region (Fig. 14, region III). These results demonstrate the importance of properly representing midtropospheric APs in studies aiming to understand the microphysical effects of aerosols on clouds systems, as has been shown by Fridlind et al. (2004) and Lebo (2014). While insights are gained from this manuscript through comparing responses between two case study realizations, assessing an ensemble of case study realizations (i.e., perturbations to initial or boundary conditions) could further assist in determining the robustness of aerosol responses observed within deep convective cloud system simulations. Furthermore, this manuscript used the presence of newly activated cloud droplets in the midtropospheric convective updrafts to assess the relative amount of updraft entrainment between two MCS events, and additional studies that can be completed on smaller domains and at large-eddy-simulation scales can be used to more thoroughly study differences in convective updraft entrainment under varying environmental conditions (e.g., wind shear).

Feedbacks between the microphysics and dynamics can further complicate the interactions between aerosol particles and precipitation processes. For the 20 May event, the CLE simulation had lower evaporation rates, which caused weaker cold pools and a structural change to the MCS in that simulation. Such strong feedbacks to the MCS structure were not discernable in the mature stage of 24 May simulations, further highlighting that aerosol-induced responses in cloud systems are often case specific and nonlinear. Last, this study has demonstrated that aerosol-induced precipitation changes within LLTS MCSs can vary depending on the region within the MCS (i.e., distance from the leading cold pool boundary) that is impacted by changing aerosol concentrations, and therefore, assessing aerosol impacts along the primary airflows within cloud systems can provide a more unified theory of aerosol–precipitation interactions.

*Acknowledgments.* This work was supported by the Department of Energy under Grant DE-SC0010569. The simulation data are available upon request from

Peter J. Marinescu (peter.marinescu@colostate.edu). The Navy Aerosol Analysis and Prediction System (NAAPS) data that were used in this study were originally accessed online (from [www.datafed.net](http://www.datafed.net)) and are now available upon request from Peter J. Marinescu. An updated NAAPS reanalysis product can also be accessed by contacting Peng Xian of the Naval Research Laboratory's Aerosol and Radiation Section. The surface CCN and UHSAS aerosol concentration data were accessed from the ARM data archive (<https://www.arm.gov/data>). CPC and navigational data were accessed via the NASA Global Hydrology Resources Center distributed data archive (<https://ghrc.nsstc.nasa.gov/home/field-campaigns/mc3e>). Andrew Heymsfield (NCAR) and Michael Poellot (University of North Dakota) were the principal investigators in the archiving of these data. Jason Tomlinson (PNNL) is acknowledged for processing and archiving of the UHSAS data.

#### REFERENCES

- Albrecht, B. A., 1989: Aerosols, cloud microphysics, and fractional cloudiness. *Science*, **245**, 1227–1230, doi:10.1126/science.245.4923.1227.
- Andrews, E., P. J. Sheridan, J. A. Ogren, and R. Ferrare, 2004: In situ aerosol profiles over the Southern Great Plains cloud and radiation test bed site: 1. Aerosol optical properties. *J. Geophys. Res.*, **109**, D06208, doi:10.1029/2003JD004025.
- Benjamin, T. B., 1968: Gravity currents and related phenomena. *J. Fluid Mech.*, **31**, 209–248, doi:10.1017/S0022112068000133.
- Bryan, G. H., and H. Morrison, 2012: Sensitivity of a simulated squall line to horizontal resolution and parameterization of microphysics. *Mon. Wea. Rev.*, **140**, 202–225, doi:10.1175/MWR-D-11-00046.1.
- , J. C. Wyngaard, and J. M. Fritsch, 2003: Resolution requirements for the simulation of deep moist convection. *Mon. Wea. Rev.*, **131**, 2394–2416, doi:10.1175/1520-0493(2003)131<2394:RRFTSO>2.0.CO;2.
- , J. C. Knievel, and M. D. Parker, 2006: A multimodel assessment of RKW theory's relevance to squall-line characteristics. *Mon. Wea. Rev.*, **134**, 2772–2792, doi:10.1175/MWR3226.1.
- Charba, J., 1974: Application of gravity current model to analysis of squall-line gust front. *Mon. Wea. Rev.*, **102**, 140–156, doi:10.1175/1520-0493(1974)102<0140:AOGCMT>2.0.CO;2.
- Cotton, W. R., and Coauthors, 2003: RAMS 2001: Current status and future directions. *Meteor. Atmos. Phys.*, **82**, 5–29, doi:10.1007/s00703-001-0584-9.
- DeMott, P. J., and Coauthors, 2010: Predicting global atmospheric ice nuclei distributions and their impacts on climate. *Proc. Natl. Acad. Sci. USA*, **107**, 11 217–11 222, doi:10.1073/pnas.0910818107.
- Doswell, C. A., H. E. Brooks, and R. A. Maddox, 1996: Flash flood forecasting: An ingredients-based methodology. *Weather Forecasting*, **11**, 560–581, doi:10.1175/1520-0434(1996)011<0560:FFFAIB>2.0.CO;2.
- Duncan, B. N., R. V. Martin, A. C. Staudt, R. Yevich, and J. A. Logan, 2003: Interannual and seasonal variability of biomass burning emissions constrained by satellite observations. *J. Geophys. Res.*, **108**, 4040, doi:10.1029/2002JD002378.
- Engerer, N. A., D. J. Stensrud, and M. C. Coniglio, 2008: Surface characteristics of observed cold pools. *Mon. Wea. Rev.*, **136**, 4839–4849, doi:10.1175/2008MWR2528.1.

- Fan, J., Y. Wang, D. Rosenfeld, and X. Liu, 2016: Review of aerosol–cloud interactions: Mechanisms, significance, and challenges. *J. Atmos. Sci.*, **73**, 4221–4252, doi:10.1175/JAS-D-16-0037.1.
- Fovell, R. G., and Y. Ogura, 1988: Numerical simulation of a midlatitude squall line in two dimensions. *J. Atmos. Sci.*, **45**, 3846–3879, doi:10.1175/1520-0469(1988)045<3846:NSOAMS>2.0.CO;2.
- Fridlind, A. M., and Coauthors, 2004: Evidence for the predominance of mid-tropospheric aerosols as subtropical anvil cloud nuclei. *Science*, **304**, 718–722, doi:10.1126/science.1094947.
- , and Coauthors, 2017: Derivation of aerosol profiles for MC3E convection studies and use in simulations of the 20 May squall line case. *Atmos. Chem. Phys.*, **17**, 5947–5972, doi:10.5194/acp-17-5947-2017.
- Fritsch, J. M., R. J. Kane, and C. R. Chelius, 1986: The contribution of mesoscale convective weather systems to the warm-season precipitation in the United States. *J. Climate Appl. Meteor.*, **25**, 1333–1345, doi:10.1175/1520-0450(1986)025<1333:TCOMCW>2.0.CO;2.
- Gebhart, K. A., S. M. Kreidenweis, and W. C. Malm, 2001: Back-trajectory analyses of fine particulate matter measured at Big Bend National Park in the historical database and the 1996 scoping study. *Sci. Total Environ.*, **276**, 185–204, doi:10.1016/S0048-9697(01)00779-3.
- Heymsfield, A. J., A. Bansemer, and M. Poellot, 2014: GPM ground validation NCAR cloud microphysics particle probes MC3E. NASA Global Hydrology Resource Center Distributed Active Archive Center, accessed 21 July 2014, <http://ghrc.nsstc.nasa.gov/>.
- Houze, R. A., 1977: Structure and dynamics of a tropical squall-line system. *Mon. Wea. Rev.*, **105**, 1540–1567, doi:10.1175/1520-0493(1977)105<1540:SADOAT>2.0.CO;2.
- Jensen, M. P., and Coauthors, 2016: The Midlatitude Continental Convective Clouds Experiment (MC3E). *Bull. Amer. Meteor. Soc.*, **97**, 1667–1686, doi:10.1175/BAMS-D-14-00228.1.
- Kunkel, K. E., S. A. Changnon, and J. R. Angel, 1994: Climatic aspects of the 1993 upper Mississippi River basin flood. *Bull. Amer. Meteor. Soc.*, **75**, 811–822, doi:10.1175/1520-0477(1994)075<0811:CAOTUM>2.0.CO;2.
- Lebo, Z. J., 2014: The sensitivity of a numerically simulated idealized squall line to the vertical distribution of aerosols. *J. Atmos. Sci.*, **71**, 4581–4596, doi:10.1175/JAS-D-14-0068.1.
- , and H. Morrison, 2014: Dynamical effects of aerosol perturbations on simulated idealized squall lines. *Mon. Wea. Rev.*, **142**, 991–1009, doi:10.1175/MWR-D-13-00156.1.
- , and —, 2015: Effects of horizontal and vertical grid spacing on mixing in simulated squall lines and implications for convective strength and structure. *Mon. Wea. Rev.*, **143**, 4355–4375, doi:10.1175/MWR-D-15-0154.1.
- Li, G., Y. Wang, K.-H. Lee, Y. Diao, and R. Zhang, 2009: Impacts of aerosols on the development and precipitation of a mesoscale squall line. *J. Geophys. Res.*, **114**, D17205, doi:10.1029/2008JD011581.
- Lynch, P., and Coauthors, 2016: An 11-year global gridded aerosol optical thickness reanalysis (v1.0) for atmospheric and climate sciences. *Geosci. Model Dev.*, **9**, 1489–1522, doi:10.5194/gmd-9-1489-2016.
- Lyons, W. A., T. E. Nelson, E. R. Williams, J. Cramer, and T. Turner, 1998: Enhanced positive cloud-to-ground lightning in thunderstorms ingesting smoke from fires. *Science*, **282**, 77–80, doi:10.1126/science.282.5386.77.
- Marinescu, P. J., S. C. van den Heever, S. M. Saleeby, and S. M. Kreidenweis, 2016: The microphysical contributions to and evolution of latent heating profiles in two MC3E MCSs. *J. Geophys. Res. Atmos.*, **121**, 7913–7935, doi:10.1002/2016JD024762.
- McGee, C. J., and S. C. van den Heever, 2014: Latent heating and mixing due to entrainment in tropical deep convection. *J. Atmos. Sci.*, **71**, 816–832, doi:10.1175/JAS-D-13-0140.1.
- Meyers, M. P., R. L. Walko, J. Y. Harrington, and W. R. Cotton, 1997: New RAMS cloud microphysics parameterization. Part II: The two-moment scheme. *Atmos. Res.*, **45**, 3–39, doi:10.1016/S0169-8095(97)00018-5.
- Morrison, H., 2012: On the numerical treatment of hydrometeor sedimentation in bulk and hybrid bulk–bin microphysics schemes. *Mon. Wea. Rev.*, **140**, 1572–1588, doi:10.1175/MWR-D-11-00140.1.
- Murray, N. D., R. E. Orville, and G. R. Huffines, 2000: Effect of pollution from Central American fires on cloud-to-ground lightning in May 1998. *Geophys. Res. Lett.*, **27**, 2249–2252, doi:10.1029/2000GL011656.
- Peppler, R. A., and Coauthors, 2000: ARM Southern Great Plains site observations of the smoke pall associated with the 1998 Central American fires. *Bull. Amer. Meteor. Soc.*, **81**, 2563–2591, doi:10.1175/1520-0477(2000)081<2563:ASGPSO>2.3.CO;2.
- Rogers, C. M., and K. P. Bowman, 2001: Transport of smoke from the Central American fires of 1998. *J. Geophys. Res.*, **106**, 28 357–28 368, doi:10.1029/2000JD000187.
- Rotunno, R., J. B. Klemp, and M. L. Weisman, 1988: A theory for strong, long-lived squall lines. *J. Atmos. Sci.*, **45**, 463–485, doi:10.1175/1520-0469(1988)045<0463:ATFSL>2.0.CO;2.
- Rutledge, S. A., and R. A. Houze, 1987: A diagnostic modeling study of the trailing stratiform region of a midlatitude squall line. *J. Atmos. Sci.*, **44**, 2640–2656, doi:10.1175/1520-0469(1987)044<2640:ADMSOT>2.0.CO;2.
- Saide, P. E., and Coauthors, 2015: Central American biomass burning smoke can increase tornado severity in the U.S. *Geophys. Res. Lett.*, **42**, 956–965, doi:10.1002/2014GL062826.
- , G. Thompson, T. Eidhammer, A. M. da Silva, R. B. Pierce, and G. R. Carmichael, 2016: Assessment of biomass burning smoke influence on environmental conditions for multiyear tornado outbreaks by combining aerosol-aware microphysics and fire emission constraints. *J. Geophys. Res. Atmos.*, **121**, 10 294–10 311, doi:10.1002/2016JD025056.
- Saleeby, S. M., and W. R. Cotton, 2004: A large-droplet mode and prognostic number concentration of cloud droplets in the Colorado State University Regional Atmospheric Modeling System (RAMS). Part I: Module descriptions and supercell test simulations. *J. Appl. Meteor.*, **43**, 182–195, doi:10.1175/1520-0450(2004)043<0182:ALMAPN>2.0.CO;2.
- , and —, 2008: A binned approach to cloud-droplet riming implemented in a bulk microphysics model. *J. Appl. Meteor. Climatol.*, **47**, 694–703, doi:10.1175/2007JAMC1664.1.
- , and S. C. van den Heever, 2013: Developments in the CSU-RAMS aerosol model: Emissions, nucleation, regeneration, deposition, and radiation. *J. Appl. Meteor. Climatol.*, **52**, 2601–2622, doi:10.1175/JAMC-D-12-0312.1.
- , —, P. J. Marinescu, S. M. Kreidenweis, and P. J. DeMott, 2016: Aerosol effects on the anvil characteristics of mesoscale convective systems. *J. Geophys. Res. Atmos.*, **121**, 10 880–10 901, doi:10.1002/2016JD025082.
- Schumacher, R. S., and R. H. Johnson, 2005: Organization and environmental properties of extreme-rain-producing mesoscale convective systems. *Mon. Wea. Rev.*, **133**, 961–976, doi:10.1175/MWR2899.1.
- Seigel, R. B., S. C. van den Heever, and S. M. Saleeby, 2013: Mineral dust indirect effects and cloud radiative feedbacks of a simulated idealized nocturnal squall line. *Atmos. Chem. Phys.*, **13**, 4467–4485, doi:10.5194/acp-13-4467-2013.
- Sheridan, P. J., D. J. Delene, and J. A. Ogren, 2001: Four years of continuous surface aerosol measurements from the Department of Energy’s Atmospheric Radiation Measurement Program Southern Great Plains Cloud and Radiation

- Testbed site. *J. Geophys. Res.*, **106**, 20735–20747, doi:10.1029/2001JD000785.
- Smull, B. F., and R. A. Houze, 1985: A midlatitude squall line with a trailing region of stratiform rain: Radar and satellite observations. *Mon. Wea. Rev.*, **113**, 117–133, doi:10.1175/1520-0493(1985)113<0117:AMSLWA>2.0.CO;2.
- Stevenson, S. N., and R. S. Schumacher, 2014: A 10-year survey of extreme rainfall events in the central and eastern United States using gridded multisensor precipitation analyses. *Mon. Wea. Rev.*, **142**, 3147–3162, doi:10.1175/MWR-D-13-00345.1.
- Tao, W.-K., X. Li, A. Khain, T. Matsui, S. Lang, and J. Simpson, 2007: Role of atmospheric aerosol concentration on deep convective precipitation: Cloud-resolving model simulations. *J. Geophys. Res.*, **112**, D24S18, doi:10.1029/2007JD008728.
- , J. Chen, Z. Li, C. Wang, and C. Zhang, 2012: Impact of aerosols on convective clouds and precipitation. *Rev. Geophys.*, **50**, RG2001, doi:10.1029/2011RG000369.
- Tomlinson, J., A. Neumann, and M. Poellot, 2012: Midlatitude Continental Convective Clouds Experiment (MC3E): Airborne instruments—Ultra-high sensitivity aerosol spectrometer. ARM Data Archive, accessed 21 July 2014, <https://www.arm.gov/data>.
- Trier, S. B., C. A. Davis, D. A. Ahijevych, M. L. Weisman, and G. H. Bryan, 2006: Mechanisms supporting long-lived episodes of propagating nocturnal convection within a 7-day WRF Model simulation. *J. Atmos. Sci.*, **63**, 2437–2461, doi:10.1175/JAS3768.1.
- Wakimoto, R. M., 1982: The life cycle of thunderstorm gust fronts as viewed with Doppler radar and rawinsonde data. *Mon. Wea. Rev.*, **110**, 1060–1082, doi:10.1175/1520-0493(1982)110<1060:TLCOTG>2.0.CO;2.
- Walko, R. L., W. R. Cotton, M. P. Meyers, and J. Y. Harrington, 1995: New RAMS cloud microphysics parameterization part I: The single-moment scheme. *Atmos. Res.*, **38**, 29–62, doi:10.1016/0169-8095(94)00087-T.
- Wang, J., S. A. Christopher, U. S. Nair, J. S. Reid, E. M. Prins, J. Szykman, and J. L. Hand, 2006: Mesoscale modeling of Central American smoke transport to the United States: 1. “Top-down” assessment of emission strength and diurnal variation impacts. *J. Geophys. Res.*, **111**, D05S17, doi:10.1029/2005JD006416.
- , S. C. van den Heever, and J. S. Reid, 2009: A conceptual model for the link between Central American biomass burning aerosols and severe weather over the south central United States. *Environ. Res. Lett.*, **4**, 15003, doi:10.1088/1748-9326/4/1/015003.
- Watson, A. I., J. Meitín, and J. B. Cunnig, 1988: Evolution of the kinematic structure and precipitation characteristics of a mesoscale convective system on 20 May 1979. *Mon. Wea. Rev.*, **116**, 1555–1567, doi:10.1175/1520-0493(1988)116<1555:EOTKSA>2.0.CO;2.
- Witek, M. L., P. J. Flatau, P. K. Quinn, and D. L. Westphal, 2007: Global sea-salt modeling: Results and validation against multicampaign shipboard measurements. *J. Geophys. Res.*, **112**, D08215, doi:10.1029/2006JD007779.